9994–10014 *Nucleic Acids Research, 2015, Vol. 43, No. 20* *Published online 17 September 2015*
doi: 10.1093/nar/gkv930

Architecture of the eIF2B regulatory subcomplex and its implications for the regulation of guanine nucleotide exchange on eIF2

Bernhard Kuhle*, Nora K. Eulig and Ralf Ficner

Abteilung für Molekulare Strukturbiologie, Institut für Mikrobiologie und Genetik, Göttinger Zentrum für Molekulare Biowissenschaften, Georg-August-Universität Göttingen, D-37077 Göttingen, Germany

Received April 21, 2015; Revised August 21, 2015; Accepted September 07, 2015

ABSTRACT

Eukaryal translation initiation factor 2B (eIF2B) acts as guanine nucleotide exchange factor (GEF) for eIF2 and forms a central target for pathways regulating global protein synthesis. eIF2B consists of five non-identical subunits (α–ϵ), which assemble into a catalytic subcomplex (γ, ϵ) responsible for the GEF activity, and a regulatory subcomplex (α, β, δ) which regulates the GEF activity under stress conditions. Here, we provide new structural and functional insight into the regulatory subcomplex of eIF2B (eIF2B^{RSC}). We report the crystal structures of eIF2Bβ and eIF2Bδ from *Chaetomium thermophilum* as well as the crystal structure of their tetrameric eIF2B$(\beta\delta)_2$ complex. Combined with mutational and biochemical data, we show that eIF2B^{RSC} exists as a hexamer in solution, consisting of two eIF2Bβδ heterodimers and one eIF2Bα_2 homodimer, which is homologous to homohexameric ribose 1,5-bisphosphate isomerases. This homology is further substantiated by the finding that eIF2Bα specifically binds AMP and GMP as ligands. Based on our data, we propose a model for eIF2B^{RSC} and its interactions with eIF2 that is consistent with previous biochemical and genetic data and provides a framework to better understand eIF2B function, the molecular basis for Gcn$^-$, Gcd$^-$ and VWM/CACH mutations and the evolutionary history of the eIF2B complex.

INTRODUCTION

Eukaryal translation initiation factor 2B (eIF2B) is the guanine nucleotide exchange factor (GEF) for the heterotrimeric translational GTPase eIF2. During each round of translation initiation GTP-bound eIF2 forms a stable ternary complex (TC) with the methionylated initiator tRNA (Met-tRNA$_i$) in order to deliver it to the 40S ribosomal subunit. Following start codon recognition on the mRNA, eIF2 hydrolyzes the bound GTP molecule and is released from the 40S subunit and Met-tRNA$_i$ in its GDP-bound state. To reenter a new round of translation initiation eIF2 has to be recycled back to its active GTP-bound state. This critical step in the nucleotide cycle of eIF2, namely the exchange of GDP for GTP, is catalyzed by eIF2B (1,2).

In comparison to GEFs of other Ras-related GTPases, eIF2B exhibits an unusually complex quaternary structure. It comprises five non-identical subunits (α–ϵ) which are thought to form two distinct subcomplexes that independently bind eIF2 (3). eIF2Bγ and -ϵ form a catalytic subcomplex that mediates the actual nucleotide exchange reaction. The remaining subunits (eIF2Bα, -β and -δ) are homologous to each other and form the so-called regulatory subcomplex (in the following eIF2B^{RSC}) (3). Although the reason for this complexity is unclear, it is believed to be linked to the regulatory role of eIF2B during translation initiation (4). Due to its importance for the nucleotide cycle of eIF2, regulation of the GEF activity of eIF2B plays a central role in the control of global protein synthesis as part of the integrated stress response (ISR) (5,6). One of the best studied examples for such a regulation mechanism is the phosphorylation of serine 51 in eIF2α (6–8), which results in a significantly increased affinity of eIF2(α-P) for eIF2B. Thereby, phosphorylation converts eIF2 from a substrate into a competitive inhibitor of its own GEF, giving rise to nonproductive eIF2(α-P)-eIF2B complexes (3,7,9,10). As a consequence, inhibition of eIF2B reduces the cellular level of TCs that are available for translation initiation, thus causing the down-regulation of global protein synthesis. At the same time eIF2(α-P) causes the up-regulation of certain mRNAs *via* a mechanism called translation re-initiation through upstream open reading frames in the 5′-leader region. E.g. expression of the transcription factor GCN4 in *Saccharomyces cerevisiae* is up-regulated due to eIF2α phosphorylation by the kinase GCN2 in response to amino-acid starvation, which in turn stimulates the expression of enzymes involved in amino-acid synthesis (6,8).

*To whom correspondence should be addressed. Tel: +49 551 39 14079; Fax: +49 551 39 14082; Email: bkuhle@gwdg.de

Over the last decades, genetic and biochemical studies identified a large number of mutations in all five eIF2B subunits that are linked to the activity of eIF2B and its sensitivity to eIF2α phosphorylation in response to stress conditions. On the one hand, a number of mutations were identified that prevent expression of *GCN4* even under stress by rendering eIF2B insensitive to inactivation by eIF2(α-P), resulting in a phenotype called general control non-derepressible (Gcn$^-$). Mutations conferring a Gcn$^-$ phenotype were found in eIF2Bα, -β and -δ of the regulatory subcomplex, which suggests that all three subunits are critical for eIF2B regulation by eIF2(α-P) (6,11). On the other hand, mutations that decrease the GEF activity of eIF2B and thereby lower cellular TC concentration (resulting in *GCN4* derepression independently of eIF2α phosphorylation and amino-acid starvation) cause a general control derepression (Gcd$^-$) phenotype in yeast. Gcd$^-$ mutations have been found for all five eIF2B subunits (12–14). Similarly, over 70 mutations were identified in mammalian eIF2B that decrease the GEF activity of eIF2B either directly by affecting the exchange reaction or indirectly by reducing the cellular levels of the exchange factor. In human a number of these mutants are associated with a genetic neurodegenerative disorder called childhood ataxia with CNS hypomyelination (CACH) or leukoencephalopathy with vanishing white matter (VWM) disease (5,15,16), thus giving a dramatic demonstration of the importance of eIF2B for cellular function.

Despite considerable efforts to understand structure and function of eIF2B, the architecture of the eIF2B complex remains elusive. Only recently it was demonstrated that yeast and mammalian eIF2B are even more complex than previously thought and exist as functional decamers rather than pentamers in solution, composed of two eIF2Bαβγδϵ hetero-pentamers with a combined molecular weight of ∼600 kDa (17,18). Within this complex, high-resolution structural information is limited to the ∼20 kDa catalytic CTD of eIF2Bϵ (19) and the human (*hs*) eIF2Bα subunit (20). The way in which the individual subunits are arranged within the decamer and how the contact between the two pentamers is mediated remains unclear (18,21). Necessarily, this lack of knowledge hampers the interpretation of the large body of available biochemical and genetic data at the molecular level. Hence, detailed structural information for the eIF2B complex is of paramount importance to provide answers to open questions regarding the origin of the unusual complexity of eIF2B as multifunctional GEF of eIF2, the molecular basis for Gcn$^-$, Gcd$^-$ and VWM/CACH phenotypes or the mechanism by which eIF2B discriminates between productive binding of eIF2 as substrate and non-productive binding of its competitive inhibitor eIF2(α-P).

The primary aim of this work was to address these questions by providing structural insight into the architecture of eIF2B^{RSC}. We solved the high-resolution crystal structures of eIF2Bβ$^{\Delta 123–148}$ and eIF2Bδ$^{148–443}$ from *Chaetomium thermophilum*, which together with the previously solved structure of *hs*eIF2Bα provide a complete set of structures for the eIF2B^{RSC}. Moreover, we solved the crystal structure of the complex between *ct*eIF2Bβ and -δ. These structures in combination with pull-down experiments, analytical size exclusion chromatography, multi angle light scattering and mutational analyses demonstrate that eIF2Bβ and eIF2Bδ form a stable tetramer which provides an extensive composite binding surface for the association of one eIF2Bα$_2$ dimer. Hence, the eIF2B^{RSC} forms a hexameric eIF2Bα$_2$(βδ)$_2$ core-complex which is structurally closely related to the homo-hexameric ribose 1,5-bisphosphate isomerase from *Thermococcus kodakarensis* (*tk*RBPI). Importantly, our structural model for eIF2B^{RSC} provides an explanatory framework for the molecular basis of Gcn$^-$, Gcd$^-$ and VWM/CACH mutations and is thus consistent with previous empirical data. On this basis, we propose a molecular mechanism by which the eIF2B^{RSC} discriminates between eIF2 as substrate and its competitive inhibitor eIF2(α-P). Finally we could show that eIF2Bα specifically binds various sugar phosphate ligands, including AMP and GMP, in the same binding pocket used by RBPIs to bind the substrate ribose 1,5-bisphosphate. Based on this observation we hypothesize that the eIF2B^{RSC} evolved from a *tk*RBPI-like metabolic enzyme which was refunctionalized to act in translation initiation as allosterically regulated metabolic sensor for the energy state of the cell. The concrete implications of this hypothesis for the regulation mechanism of extant eIF2B are discussed.

MATERIALS AND METHODS

Cloning, protein expression and purification

Cloning and mutagenesis of all *C. thermophilum* eIF2Bα, -β and -δ constructs were performed using standard procedures as described in detail in the Supplementary Materials and Methods. All constructs were expressed in *E. coli* BL21(DE3) Rosetta II cells (Novagene). eIF2Bα and mutants thereof were expressed as N-terminally His-tagged fusion proteins and purified by Ni-NTA affinity chromatography and size exclusion chromatography. His-tags were removed from all constructs by proteolytic cleavage. Full-length eIF2Bβ, eIF2Bβ$^{\Delta 123–148}$, full-length eIF2Bδ, eIF2Bδ$^{130\text{-}C}$ and all their mutants were expressed as N-terminal GST-fusions and purified by GSH-sepharose and size exclusion chromatography. Unless the protein was used in GST-pull-down experiments, the GST-tag was removed from all constructs by proteolytic cleavage. A spontaneously occurring ∼37 kDa degradation product of eIF2Bδ, which contained residues 128–466 according to MS analysis, was purified in addition to the full-length protein and used in the crystallization trials (see below). Details about the expression and purification procedures are given in the Supplementary Materials and Methods.

Protein crystallization and structure determination

eIF2Bβ. Crystallization trials for full-length eIF2Bβ and eIF2Bβ$^{\Delta 123–148}$ were performed by sitting-drop vapor diffusion with commercially available standard screens. No crystals were obtained for full-length eIF2Bβ. Crystals of eIF2Bβ$^{\Delta 123–148}$ were obtained with 9.5 mg/ml protein at 20°C in a condition containing 100 mM HEPES (pH 6.8) and 1.33 M tri-sodium citrate. X-ray diffraction data were collected at BL 14.1 at BESSY (HZB, Berlin) (22). The

phase problem was solved by molecular replacement using the program PHASER (23). The structure was refined in trigonal space group R3 at a resolution of 2.54 Å using the program PHENIX (24). Missing regions of the peptide chain were built manually in Coot (25). The final model contains two molecules per asymmetric unit (Table 1). For details see Supplementary Materials and Methods.

eIF2Bδ$^{148–443}$. Crystallization trials for eIF2Bδ were performed by sitting-drop vapor diffusion with commercially available standard screens. With a truncated version of eIF2Bδ (37 kDa fragment) diffraction quality crystals were obtained in 100 mM MES (pH 6.2) and 0.8 M $(NH_4)_2SO_4$. X-ray diffraction data were collected at BL 14.1 at BESSY (HZB, Berlin) (22). The phase problem was solved by molecular replacement using PHASER (23). The structure was refined in primitive orthorhombic space group $P2_12_12_1$ at a resolution of 2.55 Å using the program PHENIX (24). The final model contains two molecules per asymmetric unit (Table 1). For more details see Supplementary Materials and Methods.

Crystallization of the eIF2B(βδ)$_2$ complex. Initial crystals of the eIF2Bβδ complex (both proteins were purified as full-length constructs) were obtained by sitting-drop vapor diffusion in a condition containing 0.1 M MES (pH 6.5) and 22% pentaerythritol propoxylate (5/4 PO/OH) at 20°C. After optimization, crystals used for data collection were obtained in 0.1 M MES (pH 6.0), 300 mM NaCl and 32% pentaerythritol propoxylate (5/4 PO/OH) at 20°C with 4 mg/ml of protein complex (in 100 mM KCl; 10 mM NaCl; 20 mM K-phophate buffer (pH 7.5); 2 mM DTT). X-ray diffraction data used for structure determination were collected at beamline ID23–1 at ESRF (Grenoble). The phase problem was solved by molecular replacement using PHASER (23) with the atomic coordinates of *ct*eIF2Bβ$^{\Delta 123–148}$ and *ct*eIF2Bδ$^{148–443}$ as search models. The structure was refined in trigonal space group $P3_221$ at a resolution of 3.0 Å using the program PHENIX (24). Missing regions of the peptide chains were built manually in Coot (25). The final model contains two copies of *ct*eIF2Bβ and two copies of *ct*eIF2Bδ (see Table 1 for details of data collection and refinement).

Interaction studies by analytical size exclusion chromatography coupled to multi angle light scattering (SEC-MALS)

Complex formation between eIF2Bα, -β and -δ was studied by size exclusion chromatography (SEC) on an analytical Superdex 200 (10/300) column (GE Healthcare). For standard runs of the subunits, 50 μg protein in a total volume of 200 μl was loaded onto the column equilibrated in running buffer (90 mM KCl, 10 mM NaCl, 20 mM Tris/HCl (pH 7.5) and 2 mM DTT). For the analysis of binary complex formation between two subunits, 50 μg of each protein were mixed in 200 μl running buffer and incubated for 5 min at 20°C before loading onto the column. To study complex formation between all three subunits, eIF2Bβ (50 μg) was first mixed with a ∼2-fold excess of eIF2Bα (100 μg), followed by the addition of eIF2Bδ in ∼1.5-fold excess over the β-subunit (80 μg). The mixture was incubated for 5 min at 20°C in 200 μl running buffer before loading onto the column. Runs were monitored at an absorption wavelength of 280 nm. Apparent molecular weights (MW_{app}) were estimated using a protein standard giving $MW_{app} = 10^{-0.179 \cdot V + 4.631}$ (where V is the elution volume).

The absolute molecular weight (MW) of the proteins and protein complexes was determined by multi angle light scattering (MALS). Samples were run on the SEC column, connected to a miniDAWN TREOS LS detector and an Optilab T-rEX RI detector (Wyatt Technology). MW values were calculated using the ASTRA software (Wyatt Technology).

GST pull-down assays

For each binding reaction 100 μg GST fusion protein was mixed with 2-fold molar excess of non-tagged protein in a buffer containing 90 mM KCl, 10 mM NaCl, 20 mM Tris/HCl (pH 7.5) and 2 mM DTT and incubated for 15 min with 100 μl glutathione beads. After washing four times with 1 ml buffer, the bound protein was eluted with the same buffer containing additional 30 mM reduced glutathione. Samples were analyzed by SDS-PAGE.

Thermal shift assay

For the analysis of the influence of various ligands on the thermal stability of *ct*eIF2Bα, -β or -δ, the protein was diluted in 96-microplate wells (clear Multiplate 96-well PCR plates, Bio-Rad) to a final concentration of 4 μM in 20 μl total volume. The samples consisted of 50 mM HEPES pH 7.5, 300 mM KCl, 2 mM DTT and 2x SYPRO Orange (diluted from a 5000x SYPRO Orange stock solution, Molecular Probes) and 0–2 mM of various ligands (AMP, ATP, CMP, GMP, GDP, GTP, $NADP^+$, phosphoenolpyruvic acid (PEP), ribose 5-phosphate (R5P), ribulose 1,5-bisphosphate (RuBP), glucose 6-phosphate (G6P), fructose 1,6-bisphosphate (F16BP)). The plates were then sealed with sealing tape (Bio-Rad). Subsequently, samples were subjected to thermal denaturation in a Real Time PCR cycler equipped with a CFX96 optical reaction module (Bio-Rad) by applying a temperature gradient from 293 to 368 K and a ramping rate of 1 K min^{-1}. Protein unfolding was monitored by the increase in the fluorescence of the SYPRO Orange probe, which was recorded using excitation and emission wavelengths of 492 and 516 nm, respectively. The relative fluorescence emission intensity was plotted as a function of the temperature and the T_m for each individual sample was estimated from the inflection point of the melting curve (26). Experiments were repeated independently 2–3 times.

Isothermal titration calorimetry (ITC)

The thermodynamic parameters of *ct*eIF2Bα binding to different sugar phosphates were measured using a MicroCal VP-ITC instrument (GE Healthcare). Experiments were carried out in ITC buffer (20 mM HEPES/KOH (pH 7.5), 100 mM KCl, 5% glycerol, 5 mM β-mercaptoethanol) at 20°C. 7-μl aliquots of 200–400 μM ligand were injected into the 1.42 ml cell containing 10–20 μM *ct*eIF2Bα. The heat of dilution was measured by injecting the ligand into the buffer

Table 1. Crystallization, X-ray data collection and refinement statistics for structures of *Chaetomium thermophilum* eIF2B subunits β and δ and the eIF2B(βδ)$_2$ complex

	eIF2Bβ$^{\Delta 123–148}$	eIF2Bδ$^{148–443}$	eIF2B(βδ)$_2$
Crystallization condition	100 mM HEPES (pH 6.8), 1.33 M tri-sodium citrate	100 mM MES (pH 6.2), 0.8 M $(NH_4)_2SO_4$	0.1 M MES (pH 6.0), 300 mM NaCl, 32% pentaerythritol propoxylate (5/4 PO/OH)
Temperature (°C)	20	20	20
Data collection			
Space group	R3	$P2_12_12_1$	$P3_221$
Unit cell	a = 138 Å b = 138 Å c = 146.6 Å α = 90° β = 90° γ = 120°	a = 74.8 Å b = 94.5 Å c = 107.8 Å α = 90° β = 90° γ = 90°	a = 109.4 Å b = 109.4 Å c = 119.1 Å α = 90° β = 90° γ = 120°
Molecules/asym. unit	2	2	4
Resolution (Å)	2.54 (2.63–2.54)	2.55 (2.65–2.55)	3.0 (3.18–3.0)
Observed reflections	134 799 (14 846)	93 747 (10 009)	255 181 (40 737)
Unique reflections	34 537 (3801)	25 018 (2697)	31 063 (4881)
Completeness (%)	99.9 (99.9)	97.7 (98.3)	99.6 (98.3)
$<I>/\sigma$	23.7 (2.6)	16.4 (3.0)	14.7 (2.8)
R_{sym} (%)	5.0 (58.4)	5.6 (48.1)	10.7 (69.0)
CC(1/2) (%)	–	–	99.8 (84.1)
Refinement			
R_{work} (%)	17.0	18.8	20.8
R_{free} (%)	20.3	22.7	25.5
Rmsd from standard stereochemistry			
Bond length (Å)	0.008	0.004	0.007
Bond angles (°)	1.14	0.85	1.32
Ramachandran plot statistics			
Most favored (%)	98.2	98.7	98.0
Allowed regions (%)	1.8	1.3	2.0
Disallowed regions (%)	0	0	0

Values in parentheses refer to the highest resolution shell.
R_{work} and R_{free} factors are calculated using the formula $R = \Sigma_{hkl} ||F(obs)_{hkl}| - |F(calc)_{hkl}|| / \Sigma_{hkl} |F(obs)_{hkl}|$, where $F(obs)_{hkl}$ and $F(calc)_{hkl}$ are observed and measured structure factors, respectively. R_{work} and R_{free} differ in the set of reflections they are calculated from: R_{free} is calculated for the test set, whereas R_{work} is calculated for the working set.

solution without protein; the values were then subtracted from the heat of the individual binding reactions to obtain the effective heat of binding. The final titration curves were fitted using the 'Origin' based MicroCal software, assuming one binding site per protein molecule. For each isotherm the binding stoichiometry (N), enthalpy changes (ΔH) and the association constants (K_a), were obtained by a nonlinear regression fitting procedure. These directly measured values were used to estimate the Gibbs energy (ΔG) from the relation $\Delta G = -R \cdot T \cdot \ln K_a$ and the entropy changes (ΔS) through $\Delta G = \Delta H - T \cdot \Delta S$.

RESULTS

Crystal structure of eIF2Bβ

Detailed structural information about the eIF2B^{RSC} is currently limited to its α-subunit. We therefore sought to solve structures of eIF2Bβ and eIF2Bδ from the fungus *C. thermophilum*.

Despite extensive crystallization trials we were unable to obtain crystals of full-length eIF2Bβ. To improve its crystallizability we designed the construct eIF2Bβ$^{\Delta 123–148}$ which lacks residues 123–148, a region poorly conserved among eIF2Bβ homologs and predicted to form an extended loop region (Supplementary Figure S1). Importantly, according to SEC-MALS and pull-down analysis the internal deletion in eIF2Bβ$^{\Delta 123–148}$ has no negative impact on its interactions with other components of the eIF2B^{RSC} (Supplementary Figure S4D/E). eIF2Bβ$^{\Delta 123–148}$ yielded well diffracting crystals allowing structure determination by means of molecular replacement (Table 1). The final structure, refined at 2.54 Å resolution, contains two eIF2Bβ$^{\Delta 123–148}$ molecules (molecules A and B) per asymmetric unit (Figure 1A). Like eIF2Bα (20), each monomer consists of an all α-helical N-terminal domain (NTD; residues 10–202) and a Rossmann-fold-like (RFL) C-terminal domain (CTD; residues 203–419) (in the following the residue-count for wild-type eIF2Bβ is used, ignoring the internal deletion). The NTD contains six α-helices with helices αN, α1, α3, α4 and α5 assembled around α2 through hydrophobic interactions. Residues 1–9 are not resolved in the electron density and are therefore considered to be disordered. Likewise, residues 106–180 between helices α4 and α5 are not defined in the electron density of molecule B of the asymmetric unit.

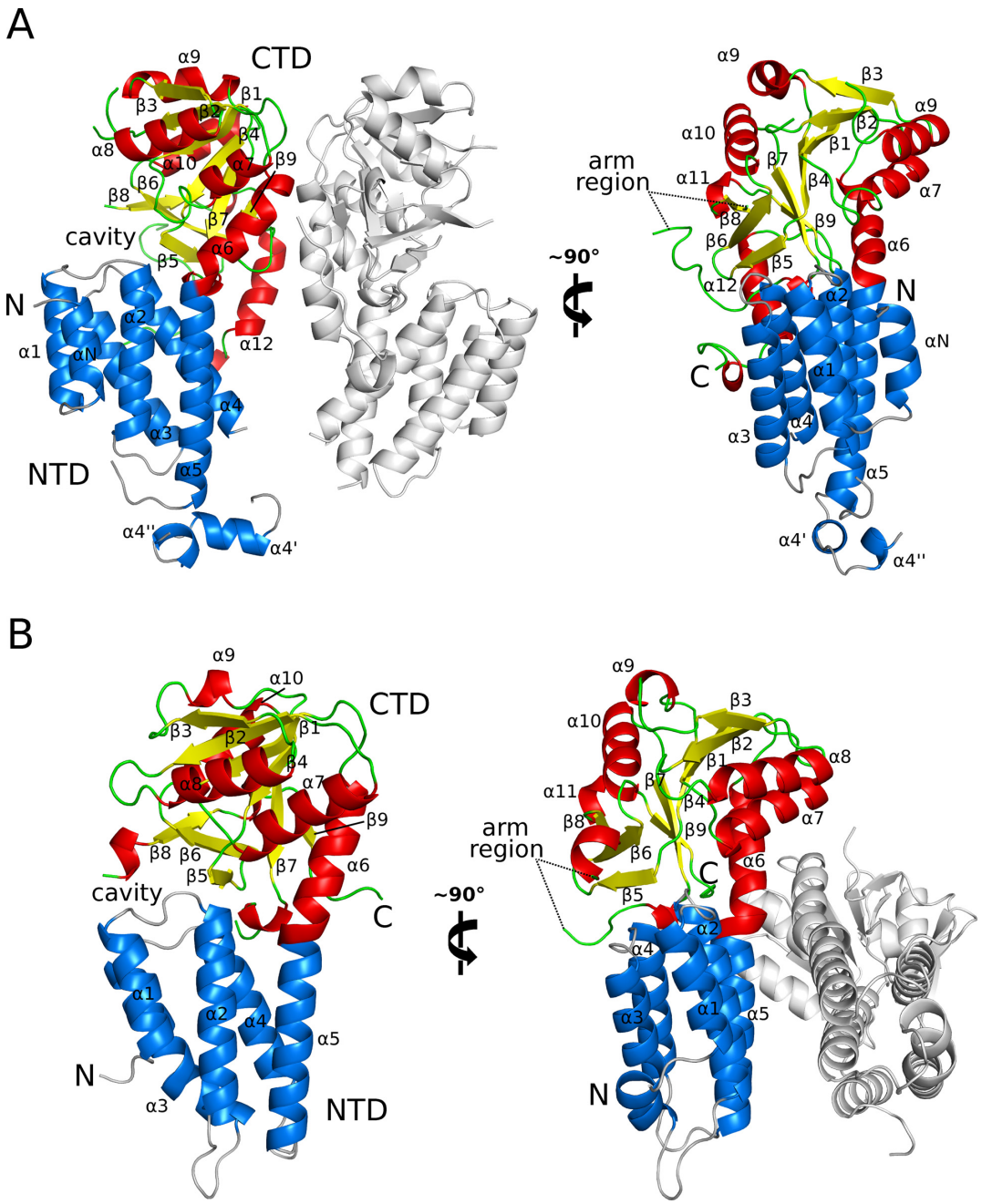

Figure 1. Crystal structures of *C. thermophilum* eIF2Bβ$^{\Delta 123–148}$ and eIF2Bδ$^{148–443}$. (**A**) Crystal structure of *ct*eIF2Bβ$^{\Delta 123–148}$ in cartoon presentation with the N-terminal α-helical domain (residues 10–202) in blue, and the helices and β-sheets of the C-terminal Rossmann-fold-like domain (residues 203–419) in red and yellow, respectively. In the left panel the second copy of eIF2Bβ in the asymmetric unit is shown in gray. (**B**) Crystal structure of *ct*eIF2Bδ$^{148–443}$ (color code as in A). The arm region and helix α12 are not resolved in the electron density. In the right panel the gray colored molecule represents the second copy of eIF2Bδ$^{148–443}$ in the asymmetric unit.

In molecule A residues 106–112 and 160–174 are not resolved, while the region comprising residues 113–122 and 149–159 (in which residues 122 and 149 are directly fused by an amide-bond) adopt two additional α-helices (α4′ and α4″) that form contacts to symmetry related molecules in the crystal packing. The C-terminal RFL domain is composed of a seven-stranded β-sheet sandwiched between six α-helices, three on each side. A second three-bladed antiparallel β-sheet (β5, β6 and β8) is packed against strands β4, β7 and β9 of the first sheet. An additional α-helix (α12) and a subsequent 11-residue loop region follow at the very C-terminus of the RFL domain, both forming direct contacts to helices α3–5 of the NTD. Two loop regions comprising residues 253–258 and 347–373 (denoted 'arm-region') are flexible and mainly disordered in the RFL domains of both molecules.

The two monomers of the asymmetric unit are arranged back-to-back, with the mainly hydrophobic dimer-interface

formed by the backside of the RFL domains (Figure 1A). N- and C-terminal domains of both molecules can be superimposed well with rmsds of 0.23 Å for 98 C_α atoms of the NTD and 0.28 Å for 145 C_α atoms of the CTD. The overall structures differ slightly more (rmsd of 0.59 Å over 270 C_α atoms) due to different angles between N- and C-terminal domains, as indicated by a slight increase in the kink between the connecting helices α5 and α6 from ∼40° in molecule A to ∼45° in B. In both molecules this kinked conformation is stabilized through the interactions of helices α3–5 in the NTD with helix α12 and the following C-terminal peptide in the CTD. As a consequence the N- and C-terminal domains form an open inter-domain cavity at the frontal face of eIF2Bβ (Figure 1A).

Crystal structure of eIF2Bδ

The crystal structure of *C. thermophilum* eIF2Bδ$^{148–443}$ was solved by molecular replacement (Table 1). The final model, refined at a resolution of 2.55 Å, contains two eIF2Bδ molecules (A and B) per asymmetric unit, both comprising residues 148–443 (Figure 1B). The two molecules superimpose well onto each other with an rmsd of 0.2 Å over 239 C_α atoms. Like eIF2Bα and eIF2Bβ, each monomer is formed by an all α-helical NTD (residues 148–266) and a C-terminal RFL domain (residues 267–443). The N-terminal 147 residues are not resolved in the electron density; SDS-PAGE and mass-spectrometry (MS) analysis of dissolved crystals indicate that most of the N-terminal region was lost prior to crystallization due to spontaneously occurring degradation of the full-length protein. The RFL domain is very similar to that described above for eIF2Bβ$^{\Delta 123–148}$. As in the β-subunit, the long presumably flexible arm-region (residues 401–420) is disordered in both molecules of the asymmetric unit. Likewise, the C-terminal 23 residues (corresponding to helix α12 and the following peptide in eIF2Bβ$^{\Delta 123–148}$) are not resolved in the electron density of eIF2Bδ$^{148–466}$. MS analysis of dissolved crystals revealed that the C-terminus of eIF2Bδ is still intact, indicating a high degree of flexibility for residues 444–466 in the crystallized protein.

The connection between N- and C-terminal domains of eIF2Bδ is formed by helices α5 and α6 that together form one long α-helix of 48 Å in length that is kinked by ∼20° in the transition from one domain to the other. As a consequence of the small angle the cavity formed between N- and C-terminal domains at the front of the protein is nearly entirely closed (Figure 1B).

Comparison between structures of eIF2Bα, -β and -δ

Earlier analyses revealed mutual sequence similarities between the three regulatory subunits eIF2Bα, -β and -δ (27). Consistently, our structural analysis for eIF2Bβ$^{\Delta 123–148}$ and eIF2Bδ from *C. thermophilum* demonstrates that the three subunits exhibit a common overall fold, comprising an N-terminal helix bundle and a C-terminal Rossmann-like fold (Figure 2A–C). This overall fold is further shared with archaeal eIF2B-like proteins (aIF2Bs) (28), 5-methylthioribose 1-phosphate isomerases (M1PIs) (29,30) and ribose 1,5-bisphosphate isomerases (RBPIs) (31) (Figure 2D–F).

With respect to its potential functional implications, one of the most prominent distinctive features among eIF2Bα/β/δ-like proteins is the kink found in the transition from helix α5 in the NTD to helix α6 of the CTD and its stabilization by helix α12 (Figure 2; see also Discussion). The angle between the axes through both helices is ∼30° in *hs*eIF2Bα and 40–45° in *ct*eIF2Bβ$^{\Delta 123–148}$, which in both cases is stabilized by the direct contacts of the NTD to the C-terminal helix α12. In eIF2Bδ$^{148–466}$ helices α5 and α6 are nearly coaxially fused with an angle of only ∼20°, a conformational state that is accompanied by the absence of the stabilizing contact to the C-terminal α-helix. This suggests that the contact to the well conserved helix α12 may play a critical role during the conformational transition between a kinked and an un-kinked state, resulting in an open or closed inter-domain cavity at the frontal face, respectively. This supposed causal connection between helix α12 and the kinked state of NTD and CTD is supported by the available structures of M1PIs, RBPIs and aIF2Bs: while aIF2B from *P. horikoshii* lacks α12 entirely (Figure 2E), M1PIs contain only a short counterpart that allows no contact to the NTD (Figure 2F); as a result, *ph*aIF2B as well as M1PIs exhibit nearly straight connecting helices between NTD and CTD. By contrast, the RBPI from *T. kodakarensis* contains a C-terminal α-helix that is structurally virtually identical to α12 in eIF2Bα and -β. Importantly, *tk*RBPI was crystallized in two conformational states: one in which α12 and the following C-terminal peptide form direct contacts to the NTD and thereby stabilize an angle of ∼50° between helices α5 and α6 (PDB: 3A11; Figure 2D); in the second structure α12 and the following C-terminal peptide have lost these contacts, accompanied by the reduction of the kink between α5 and α6 to ∼20° (PDB: 3VM6; see also Figure 8A). The question whether eIF2Bδ constitutively adopts a straight conformation as observed in the crystal structure or whether it can likewise adopt a kinked state cannot be unambiguously answered at present. The fact that eIF2Bδ orthologs contain a well conserved C-terminal region corresponding to α12 (residues 451–460) and predicted as an α-helix (Supplementary Figure S2) supports the idea that eIF2Bδ contains helix α12 and could thus adopt a kinked conformational state.

A critical consequence arising from a large or small angle between α5 and α6 is the opening or closing of the cavity formed by the N- and C-terminal domains in eIF2Bα, -β and -δ (Figure 2). In eIF2Bα this cavity allows the coordination of a sulfate ion in a pocket of the cavity ∼16 Å from its entrance (20). Sulfate ions have also been observed in the narrower cavities of several M1PIs. However, here the sulfate ions were positioned significantly closer to the entrance, coordinated by a different set of residues (20). Notably, the positions of the sulfate ions in eIF2Bα and M1PIs correspond to those of the 1′ and 5′ phosphates of the ribose 1,5-bisphosphate substrate bound in the 'closed' crystal structure of *tk*RBPI (31).

eIF2Bα forms a homodimer in solution, eIF2Bβ and eIF2Bδ are monomers

Previously studied aIF2Bs, RBPIs and M1PIs were found to form stable 'canonical' homodimers along the same dimer

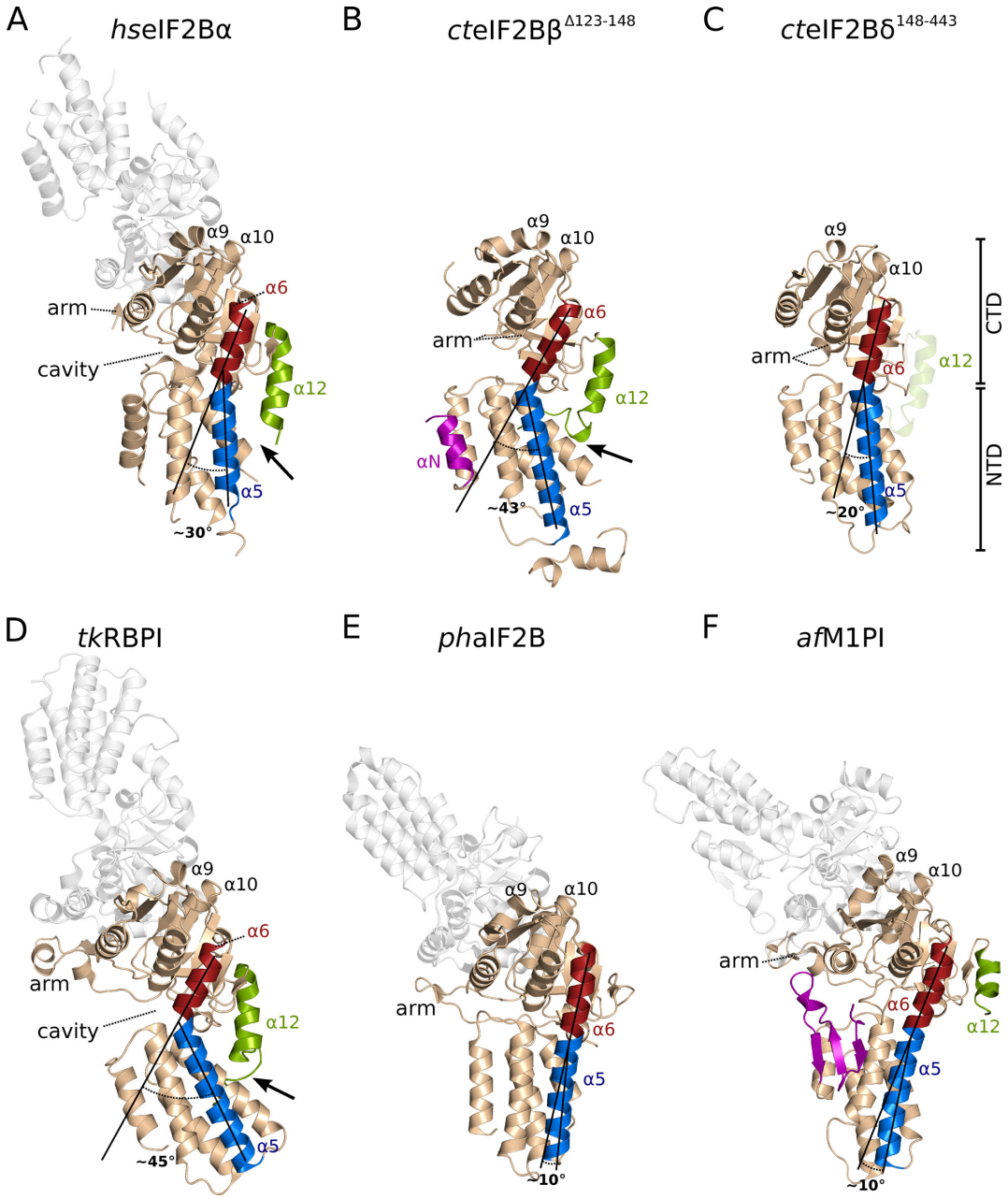

Figure 2. Comparison of *hs*eIF2Bα, *ct*eIF2Bβ and *ct*eIF2Bδ with *T. kodakarensis* RBPI (*tkRBPI*), *Pyrococcus horkoshii* aIF2B and *Archaeoglobus fulgidus* M1PI. All six proteins consist of an N-terminal helix bundle (NTD) and a C-terminal RFL domain (CTD). With the exception of *ct*eIF2Bβ$^{\Delta 123–148}$ (**B**) and *ct*eIF2Bδ$^{148–443}$ (**C**), all homologs form homodimers using helices α9, α10 and the arm-region as canonical interface for homodimerization (the second molecule is shown in gray). The structures of *hs*eIF2Bα (PDB 3ECS) (**A**), *ct*eIF2Bβ$^{\Delta 123–148}$ and *tk*RBPI (PDB 3A11) (**D**) exhibit significantly increased angles between helices α5 and α6 (colored blue and red, respectively), which are stabilized by helix α12 (green). Although *ct*eIF2Bδ$^{148–443}$ contains conserved C-terminal residues predicted to form an α helix (modeled as semitransparent helix in C), the helix is not present in the determined structure, resulting in a decreased kink between α5 and α6 and a closed inter-domain cavity. Unlike the eIF2B subunits and *tk*RBPI, *pha*IF2B (PDB 1VB5) (**E**) and *af*M1PI (PDB 1T5O) (**F**) contain either no or a significantly shorter helix α12, and show virtually no kink in helix α5/α6. The N-terminal helix αN and the β-sheet are idiosyncratic to *ct*eIF2Bβ and M1PIs, respectively (shown in purple).

interfaces involving two α-helices (α9 and α10) and a structurally conserved loop (arm-region) of the C-terminal RFL domain (Figure 2) (28,30,31). The same canonical dimer was found in the crystal structure of *hs*eIF2Bα (20), and recent biochemical studies suggest that eIF2Bα uses this interface to form a physiological homodimer in solution (18,21). It was therefore intriguing to find that the structures of eIF2Bβ$^{\Delta 123–148}$ and eIF2Bδ$^{148–443}$ constitute the first examples among eIF2Bα/β/δ-like proteins that apparently do not form stable homodimers (Figure 2). The canonical dimer interfaces instead remain unoccupied in both subunits and would thus be free for interactions with other components of eIF2B.

In order to further test this possibility, we studied the oligomeric state of the three regulatory subunits from *C. thermophilum* in solution using analytical size exclusion chromatography coupled to multi angle light scattering (SEC-MALS). In line with previous reports (18,21) we found that eIF2Bα (40.8 kDa) elutes from the SEC column (Superdex 200 10/300) at a volume of 13 ml, corresponding to an apparent molecular weight (MW_{app}) of 90 kDa as expected for a homodimer (Figure 3A). MALS experiments confirmed this result giving an absolute MW of 78 kDa. No additional peak was observed at a higher elution volume, suggesting the absence of monomers and a high stability of the eIF2Bα_2 homodimer. Two additional small eIF2Bα containing peaks eluted at smaller elution volume; MALS analysis indicated MWs of 162 kDa (11 ml) and 254 kDa (10 ml) which could correspond to the formation of small amounts of tetra- and hexamers, respectively.

eIF2Bβ (45.3 kDa) eluted at 14.8 ml from the SEC column, corresponding to an MW_{app} of 51 kDa as expected for a monomer (Figure 3B). This result was supported by the MALS experiments, yielding a MW of 41 kDa. Thus, *ct*eIF2Bβ seems to exist as a monomer in solution in agreement with the crystal structure and previous reports for the ortholog from *S. cerevisiae* (21).

Finally, full-length *ct*eIF2Bδ (49.7 kDa) eluted at 13.1 ml from the column, giving an MW_{app} of 89 kDa, suggesting a homodimer for eIF2Bδ (Figure 3C). However, MALS experiments yielded a MW of 51.9 kDa, consistent only with a monomeric state of eIF2Bδ in solution and in line with the observations from the crystal structure. The misleading migration behavior of eIF2Bδ can be explained by its extended N-terminal region (residues 1–140) that is predicted to be unstructured and would thus promote faster migration on the column. To test this assumption, a construct lacking the poorly conserved residues 1–129 (eIF2B$\delta^{130\text{-}C}$) was generated. In line with our assumption, eIF2B$\delta^{130\text{-}C}$ (37 kDa) eluted from the column at 15.1 ml, corresponding to an MW_{app} of 45 kDa and thus a monomer. This is further supported by the MALS experiments which yielded a MW of 43.6 kDa (Supplementary Figure S4A).

eIF2Bβ and eIF2Bδ form a tetrameric complex

Previous evidence indicated that eIF2Bα, -β and -δ form a stable regulatory subcomplex within eIF2B (3,9). However, despite recent advances (17,18,21) the architecture of the $eIF2B^{RSC}$ and the interactions between its individual subunits remained elusive.

Using SEC-MALS and pull-down experiments, we found that neither eIF2Bβ, nor eIF2Bδ interacts with eIF2Bα_2 in the absence of the third subunit to yield a higher-order complex (Figure 5A, lanes 6 and 10 and Supplementary Figure S4). By contrast, eIF2Bβ and eIF2Bδ interact with each other even in the absence of eIF2Bα and form a stable complex in the SEC-MALS experiments that eluted at 10.54 ml (Figure 3D), as well as in the pull-down experiments (Figure 5A, lanes 8 and 12 and Supplementary Figure S4E, lanes 5 and 6). Surprisingly, MALS indicated an absolute mass of 186 kDa rather than the expected ∼92 kDa for a heterodimer. Instead, given the apparent 1:1 stoichiometry of both proteins in the complex (Figure 3D), this result is only compatible with the formation of a tetrameric eIF2B$(\beta\delta)_2$ complex comprising two copies of each subunit (calculated mass (MW_{calc}) of 184 kDa). Hence, the two proteins not only form an eIF2Bβδ heterodimer but two of these dimers in turn interact to form a stable dimer of heterodimers.

To test whether any of the interactions within eIF2B$(\beta\delta)_2$ involve the canonical dimerization interface used for homodimerization in homologous proteins (Figure 2) we mutated surface-exposed hydrophobic residues in helices α9 and α10 of the presumed interface of both subunits, generating point mutants eIF2Bβ^{A286E} and eIF2Bδ^{M379E}. According to pull-down experiments the two mutants still formed a complex with each other (Figure 5A, lanes 9 and 13). This complex however eluted from the SEC column at 11.6 ml (Figure 3E) instead of the 10.54 ml observed for the wild-type proteins (Figure 3D); MALS revealed a MW of only 101 kDa for the eIF2B$\beta^{A286E}\delta^{M379E}$ complex. This indicates that the two mutations indeed disrupt one of the eIF2Bβ-eIF2Bδ interactions within the eIF2B$(\beta\delta)_2$ complex—most likely formed *via* the canonical dimerization interface (see below)—while a second non-canonical interface remains unaffected and gives rise to a stable non-canonical heterodimer (MW_{calc} of 92 kDa).

Crystal structure of the eIF2B$(\beta\delta)_2$ subcomplex—a dimer of canonical eIF2Bβδ heterodimers

The structure of the *C. thermophilum* eIF2B$(\beta\delta)_2$ complex was solved by means of molecular replacement and refined at a resolution of 3.0 Å (Table 1). The asymmetric unit of the crystal contains two copies of each subunit, which form a tetramer with 1:1 stoichiometry as predicted by the SEC-MALS experiments (see above). The tetramer is composed of two virtually identical canonical eIF2Bβδ heterodimers with helices α9 and α10 of both subunits forming the main dimerization interface in the same way as observed for eIF2Bα_2 (Figure 4). A286 in eIF2Bβ and M379 in eIF2Bδ lie in the center of these interfaces and are directly involved in hydrophobic interactions between the two subunits, consistent with the observation that their exchange against Glu disrupts tetramer formation (Figures 3E and 4B). Additional stabilizing contacts within the canonical heterodimer are provided by the arm-region and residues 134–137 of the N-terminal region of eIF2Bδ. Both are not visible in the isolated eIF2Bδ structure but become stabilized through interactions with the associated eIF2Bβ-RFL domain next to strand β3 (Figure 4A; inset). The rest of the N-terminal region (residues 1–126) and residues 444–466 of eIF2Bδ are not resolved in the electron density. Likewise, residues 106–180 between helices α4 and α5 in the NTD and the arm-region of eIF2Bβ are not resolved and thus seem to remain flexible even in the eIF2B$(\beta\delta)_2$ complex.

The two canonical dimers in the eIF2B$(\beta\delta)_2$ complex are arranged antiparallel to each other with 2-fold rotational symmetry. The extensive dimer-dimer interface of >1600 Å^2 buried surface area is almost exclusively formed by three conserved areas (I–III) at the backside of each RFL domain (opposite to the inter-domain cavity) (Supplementary Figure S5A): in each eIF2Bβ subunit the area between the C-termini of helices α6 and α10 and the N-

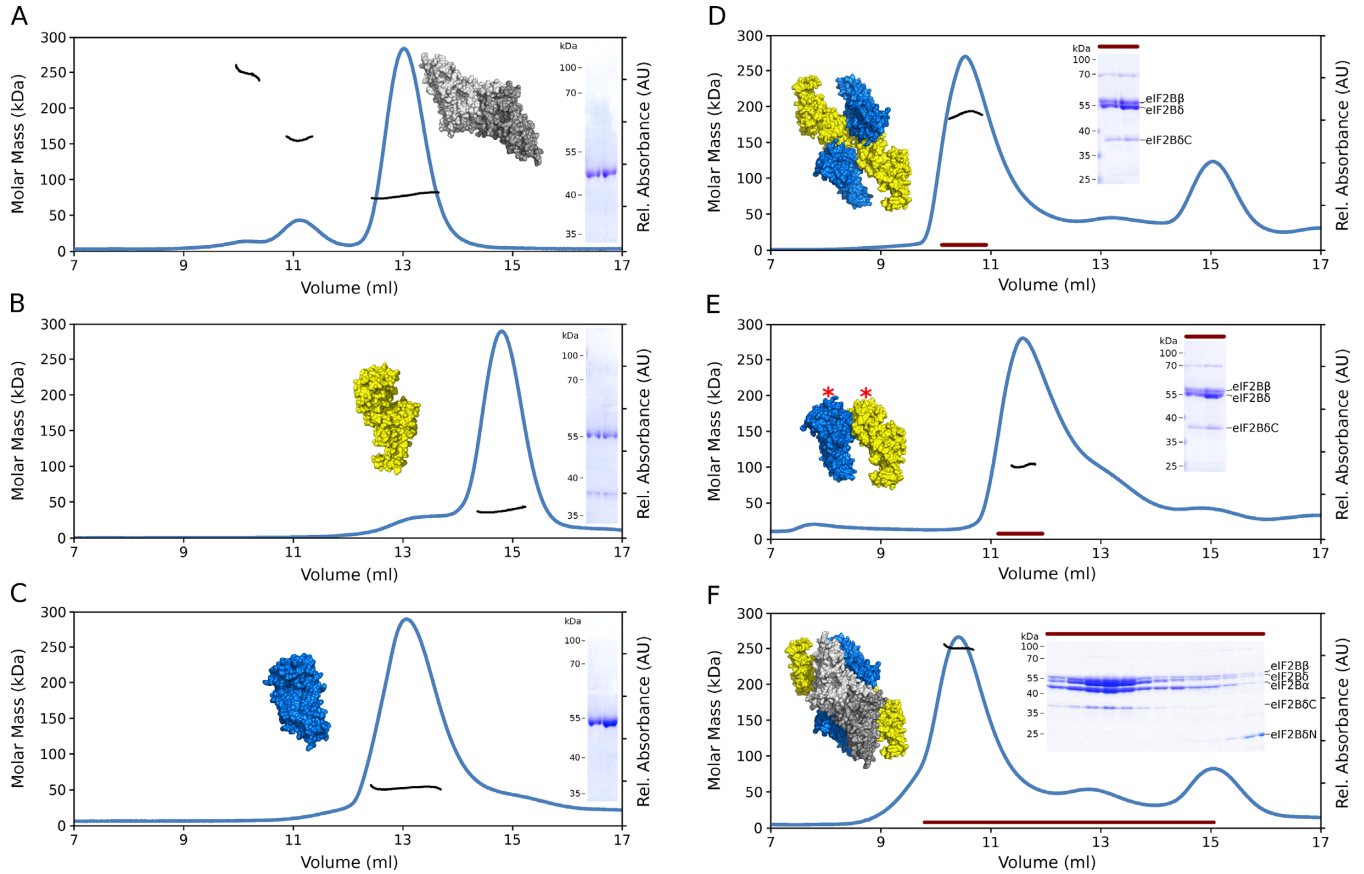

Figure 3. eIF2Bα, eIF2Bβ and eIF2Bδ from *C. thermophilum* form a hexamer. (**A**) *ct*eIF2Bα elutes from the SEC column in three peaks with molar mass distributions as calculated by MALS indicated by short black lines above/inside the peaks. The corresponding molecular weights are 254 kDa (10 ml) and 162 kDa (11 ml) for the two small peaks and 78 kDa for the main peak at 13 ml, corresponding to an eIF2Bα$_2$ dimer as found in the crystal structure (gray surface; PDB 3ECS). (**B**) *ct*eIF2Bβ elutes in one main peak at 14.8 ml. MALS yields a MW of 41 kDa, as expected for a monomer (yellow surface). (**C**) *ct*eIF2Bδ elutes in a single peak at 13.1 ml. The molar mass distribution calculated by MALS gives a MW of 51.9 kDa, consistent with eIF2Bδ being a monomer in solution (blue surface). (**D**) eIF2Bβ and eIF2Bδ form a stable complex that elutes at 10.54 ml. The molar mass distribution calculated by MALS gives an MW of 186 kDa, which corresponds to a tetramer comprising two copies of each subunit. (**E**) Interactions between *ct*eIF2Bβ^{A286E} and *ct*eIF2Bδ^{M379E}. The two mutant proteins form a stable complex that elutes at 11.6 ml. According to MALS the complex has a MW of 101 kDa, which corresponds to a heterodimeric complex formed via a non-canonical dimerization interface as shown in the surface presentation (* marks the point mutations). (**F**) *ct*eIF2Bα, -β and -δ assemble into a complex that elutes at 10.5 ml. MALS analysis yields a MW of 256 kDa. This suggests an eIF2Bα$_2$(βδ)$_2$ hexameric complex with only slightly increased radius compared to eIF2B(βδ)$_2$. The surface presentations of the complexes in (**D**) and (**E**) are based on the structure presented in Figure 4A; that in (**F**) is based on the structural model presented in Figure 6C. The coloring for the three subunits is the same as in (**A**–**C**). SDS-PAGE analyses of peak fractions are shown as insets. In (**D**–**F**) the additional bands migrating at ∼20 kDa and ∼37 kDa are due to the proteolytic cleavage of eIF2Bδ into an N-terminal (eIF2BδN) and a C-terminal fragment (eIF2BδC), respectively; the latter corresponds to the crystallized fragment shown in Figure 1B.

terminus of α12 forms a large contact surface (area I) for residues 399–409 of the arm-region, the β5-β6 loop, α11 and the N-terminus of α12 (together forming area III) in the δ-subunit of the second canonical heterodimer; this interface is complemented by residues 135–141 in the N-terminal region of eIF2Bδ (containing the conserved ^{137}FSHIP^{141} motif) which forms close contacts to the loop following helix α6 in eIF2Bβ. Moreover, the two β-subunits contact each other through a number of specific interactions in the area of helices α9 and α10 (area II), e.g. a hydrogen bond and a salt bridge from the absolutely conserved R290 in each copy of eIF2Bβ to N292 and D219 in the other copy. No contacts are formed between the two δ-subunits. Likewise, no contacts are formed between the four N-terminal domains. Significantly, six of eight Gcn$^-$ mutations in the RFL domain of eIF2Bβ map to areas I and II and are directly involved in dimer-dimer association (Figure 4A, Supplementary Figures S5A and S9D). This includes *sc*D178Y (*ct*I213), *sc*R254C (*ct*R290), *sc*P291S (*ct*P326), *sc*I348V (*ct*V385), *sc*N357I (*ct*T394) and *sc*S359G (*ct*H396). Additionally, the Gcn$^-$ sites *sc*F523I (*ct*Y409) and *sc*I625F (*ct*I434) in eIF2Bδ map to area III; *ct*Y409 lies within contact distance to *ct*I213 in eIF2Bβ (Figure 4A; inset) and *ct*I434 forms part of the hydrophobic core underneath helix α11.

Two mutants, eIF2Bβ^{I213Y,H216Y} and eIF2Bδ^{PolyAla}, were generated to assess whether mutations in either of the dimer-dimer interfaces has a negative impact on tetramer formation. In eIF2Bβ^{I213Y,H216Y} residues I213 and H216 in area I were replaced by tyrosine; in eIF2Bδ^{PolyAla} six consecutive residues at the N-terminus of the arm-region (^{400}ERVSVD^{405}) were replaced by alanine. SEC-

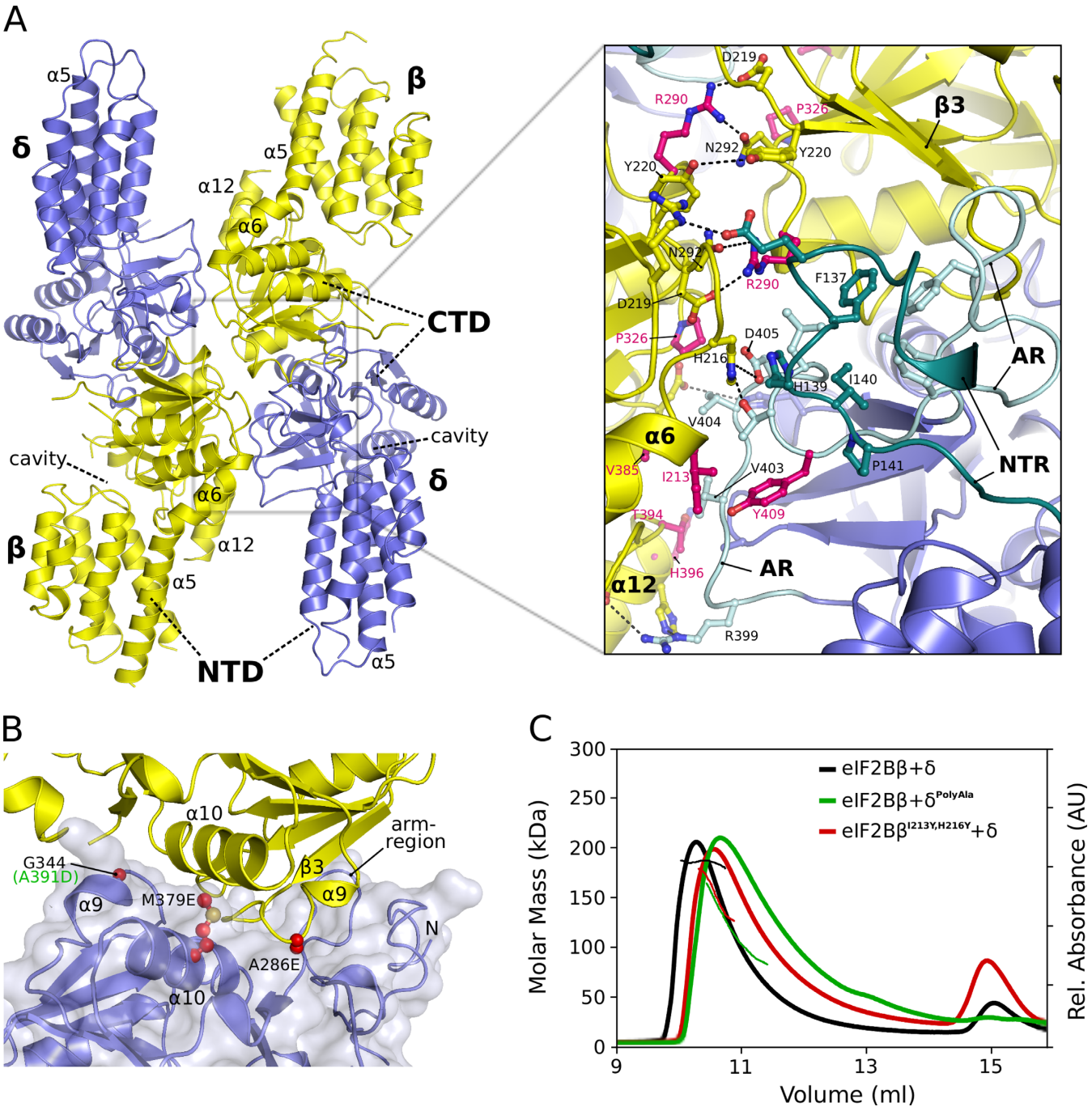

Figure 4. Crystal structure of the eIF2B$(\beta\delta)_2$ subcomplex. (**A**) Front view (onto the inter-domain cavities) of the tetrameric eIF2B$(\beta\delta)_2$ complex. eIF2Bβ and eIF2Bδ are colored yellow and blue, respectively. The complex is formed by two canonical eIF2Bβδ heterodimers in a head-to-tail arrangement, resulting in 2-fold rotational symmetry. The dimer-dimer interface is exclusively formed by the backsides of the four C-terminal domains, while the NTDs point away from each other. The inset shows details of the intricate interaction network between the two dimers, which involves both hydrophobic as well as polar interactions (indicated by dotted lines). Directly involved residues are shown as sticks; residues in pink correspond to residues altered by Gcn$^-$ mutations in the yeast orthologs (see also Supplementary Figures S1 and S2). In eIF2Bδ the N-terminal region (NTR; residues 135–141) with the conserved ^{137}FSHIP^{141} motif and the arm-region (AR) are colored in teal and light blue, respectively. (**B**) Canonical dimerization interface between eIF2Bβ (yellow) and eIF2Bδ (blue) via helices α9 and α10 and the arm-region of eIF2Bδ. Residues shown as red sticks and spheres indicate the positions of the two point mutations A286E and M379E that disrupt canonical dimerization (see also Figure 3E) as well as the VWM mutation A391D in *hs*eIF2Bδ (*ct*G344). (**C**) SEC-MALS experiments with mutations in the dimer-dimer interface of eIF2B$(\beta\delta)_2$. Unlike for the wild-type complex (black lines; MW of 186 kDa), mutations I213Y and H216Y at the end of helix α6 in eIF2Bβ (eIF2B$\beta^{I213Y,H216Y}$; red lines) or the poly-alanine mutation of ^{400}ERVSVD^{405} in the arm-region of eIF2Bδ (eIF2B$\delta^{PolyAla}$; green lines) destabilizes tetramerization, resulting in an unstable molar mass distribution for the complex peaks.

MALS experiments revealed that both eIF2Bβ^{I213Y,H216Y} and eIF2Bδ^{PolyAla} were still able to form complexes with eIF2Bδ and eIF2Bβ, respectively—as expected as the canonical dimer interface remains intact (Figure 4C). However, unlike the stable tetrameric wild-type complex (186 kDa) these complexes exhibited an unstable molar mass distribution ranging between ∼170 kDa at the beginning and ∼100 kDa at the end of the complex peaks. Thus, both mutants seem to retain their ability to form canonical heterodimers. At the same time however they destabilize (but do not abolish) formation of the tetrameric complex resulting in a mixture of dimeric and unstable tetrameric complexes.

The eIF2B^{RSC} is an eIF2Bα$_2$(βδ)$_2$ hexamer

Based on the finding that eIF2Bα exists as a homodimer, it was recently suggested that the three regulatory subunits assemble into an α$_2$(βδ)$_2$ hexamer rather than a heterotrimer, comprising one eIF2Bα$_2$ dimer and two eIF2Bβδ heterodimers (21). Direct experimental evidence for such a complex was so far missing. We therefore tested complex formation between all three subunits using SEC-MALS and pull-down experiments. The three regulatory subunits readily formed a stable complex on the SEC column as well as in pull-down experiments (Figures 3F and 5A, lanes 7 and 11; Supplementary Figure S4E, lanes 8 and 9). MALS analysis yielded a MW of 256 kDa, suggesting that the eIF2B(βδ)$_2$ complex associates with one eIF2Bα$_2$ dimer to form an α$_2$(βδ)$_2$ hexamer (MW$_{calc}$ of 265.6 kDa). Interestingly, this complex eluted from the SEC column at 10.5 ml only 0.04 ml earlier than the significantly smaller eIF2B(βδ)$_2$ complex lacking the two α-subunits (10.54 ml), indicating similar radii of gyration for the two complexes.

Structural model for the regulatory eIF2Bα$_2$(βδ)$_2$ subcomplex

In the previous sections we demonstrated how eIF2Bβ and -δ assemble into an eIF2B(βδ)$_2$ complex. This complex forms a composite surface area for the association of eIF2Bα$_2$, yielding a hexameric eIF2Bα$_2$(βδ)$_2$ regulatory subcomplex. As argued in the following, integration of our own and previously reported data provides strong evidence that this eIF2Bα$_2$(βδ)$_2$ complex is structurally homologous to the RBPI from *T. kodakarensis* (31).

The *tk*RBPI monomer is a close structural homolog of eIF2Bα/β/δ (Figure 2). Structural and biochemical studies demonstrated that *tk*RBPI assembles into a constitutive hexamer as physiological entity by the coaxial trimerization of canonical homodimers around a 3-fold rotation axis (Figure 6B) (31). Neighboring dimers are tethered together by an intricate network of interactions mediated exclusively by the three α12 helices and adjacent surfaces at the backside of each of the six C-terminal RFL domains (31). Each individual canonical dimer is thus bound by an extensive 2-fold rotation-symmmetrical interface formed by the two remaining canonical dimers. No direct intersubunit contacts occur between the axial, outward pointing NTDs.

Direct comparison shows that the eIF2B(βδ)$_2$ complex is arranged virtually identically to either two of the three homodimers in the *tk*RBPI hexamer, using homologous interfaces (areas I–III) for dimer-dimer association (compare Figure 4A and Supplementary Figure S5D). Thus, just as any two *tk*RBPI homodimers provide the composite binding surface for the third homodimer, the eIF2B(βδ)$_2$ tetramer provides a composite 2-fold rotation-symmetrical interface for the association of the canonical eIF2Bα$_2$ homodimer (Figure 6A and Supplementary Figure S5). As a consequence, the two eIF2Bβδ heterodimers and the canonical eIF2Bα$_2$ homodimer are assembled around a pseudo 3-fold rotation axis to form the hexameric eIF2Bα$_2$(βδ)$_2$ complex (Figure 6C and Supplementary Figure S5C). Each dimer is thereby bound by the extensive surfaces provided by areas I, II and III of the remaining two dimers (Figure 6A). Significantly, the proposed interface for eIF2Bα$_2$ association contains the majority of Gcn$^-$ mutations outside the dimer-dimer interface in eIF2B(βδ)$_2$, suggesting a direct role for these positions in hexamer assembly (Figure 6A, Supplementary Figures S8D and S9D). These include *sc*F240I/L (*hs*F239/*ct*T304) in area III of eIF2Bα, *sc*T291P (*hs*T292/*ct*M363) and *sc*S293R (*hs*S294/*ct*S365) in area I of eIF2Bα, *sc*Y305C (*ct*D340) and *sc*P306L (*ct*P341) in area III of eIF2Bβ as well as *sc*K627T (*ct*G436), *sc*A634D (*ct*F443), *sc*P636T (*ct*P449), *sc*P637L (*ct*A450) and *sc*P641F (*ct*L454) in area I of eIF2Bδ.

In order to assess the validity of the proposed eIF2Bα$_2$(βδ)$_2$ complex we generated four mutants replacing residues in the assumed interface for eIF2Bα$_2$ (Figure 6A/C): eIF2Bα^{Y176R} alters a conserved aromatic residue at the end of helix α6 (area I) that according to our model interacts with the N-terminal arm-region (area III) of eIF2Bβ; in eIF2Bα^{T304E,P305L,I306E} three conserved residues in the N-terminal arm-region (area III) were mutated to disrupt interactions with area I in eIF2Bδ; eIF2Bβ^{D340R,P341D} contains two point mutations in the N-terminal arm-region (area III) that are expected to destabilize its interactions with area I of eIF2Bα in the vicinity to Y176; eIF2Bδ^{S279Y} contains a point mutation at the end of helix α6 (area I) that interacts with the N-terminal arm-region (area III) of eIF2Bα in the proposed eIF2Bα$_2$(βδ)$_2$ complex. In agreement with the model pull-down experiments demonstrated that the eIF2Bβ^{D340R,P341D}δ^{S279Y} complex is unable to bind wild-type eIF2Bα$_2$ (Figure 5B, Lane 7). Likewise, the eIF2Bα^{T304E,P305L,I306E} triple mutant failed to be incorporated into the eIF2Bβδ complex (Figure 5B, Lane 8), an observation that was corroborated also by SEC-MALS experiments (Figure 5C). A less severe effect was observed for the eIF2Bα^{Y176R} mutant, which was still incorporated into eIF2Bβδ complexes, albeit at significantly reduced efficiency compared to wild-type eIF2Bα (Figure 5B, Lane 9). As shown in Lanes 10 and 11 of Figure 5B eIF2Bα^{Y176R} binding was further reduced by eIF2Bδ^{S279Y} in combination with wild-type eIF2Bβ and finally completely abolished by combining eIF2Bδ^{S279Y} with eIF2Bβ^{D340R,P341D}. Hence, these results corroborate the *tk*RBPI-like model for the association of eIF2Bα$_2$ with the eIF2B(βδ)$_2$ complex (Figure 6C).

An important consequence of the *tk*RBPI-like structural model for eIF2Bα$_2$(βδ)$_2$ is the mutual cooperativity in internal stabilization of the hexamer. Each dimer bridges and thereby stabilizes the canonical as well as non-canonical

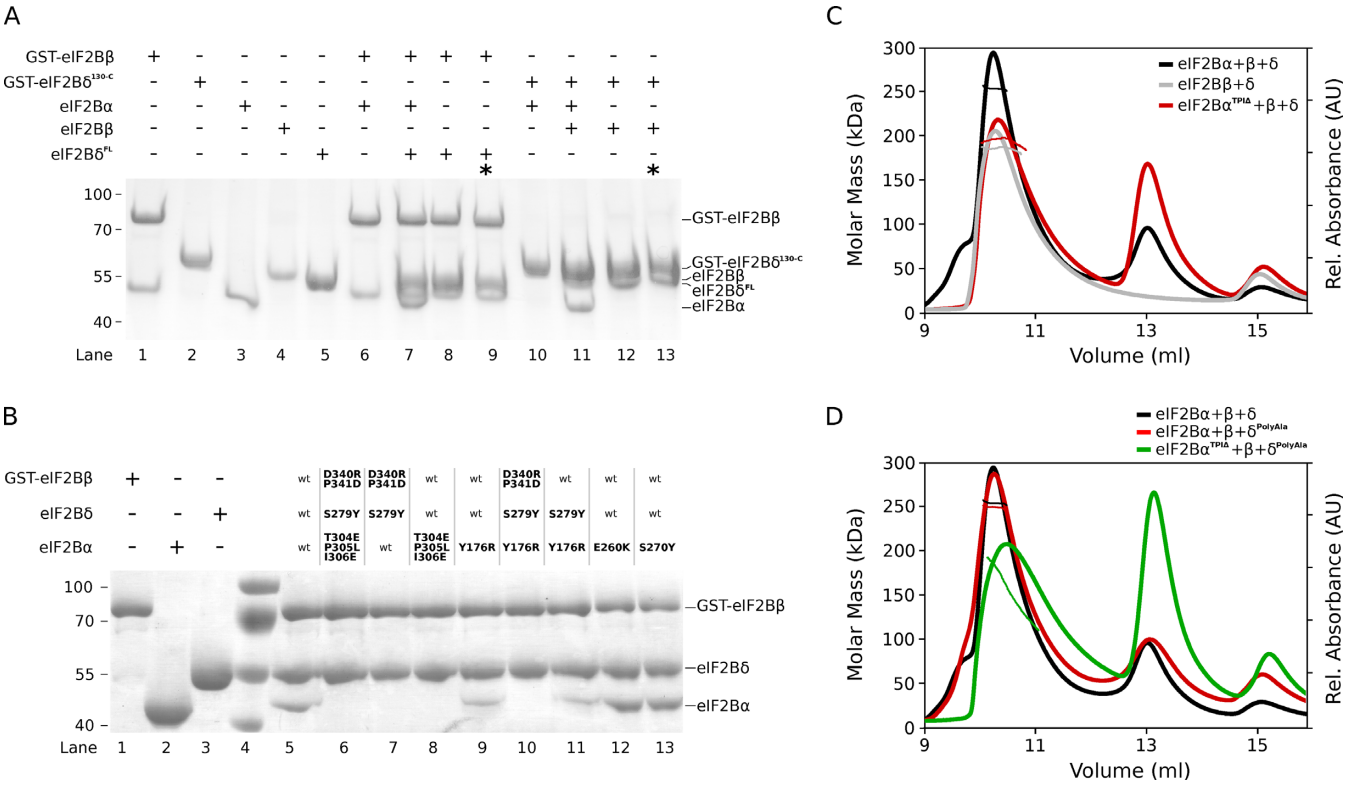

Figure 5. Interactions between wild-type and mutant forms of *ct*eIF2Bα, -β and -δ. (**A**) GST pull-down between eIF2Bα, -β and -δ. Lanes 1–5 show the isolated proteins as reference (in lane 1 the band below the 55 kDa marker is a GST-containing degradation product of GST-eIF2Bβ). Lanes 6–8 show the elution fractions (after the removal of unbound proteins by extensive washing) for the pull-down experiments of GST-tagged eIF2Bβ with eIF2Bα (Lane 6), with eIF2Bα and -δ (7), and with eIF2Bδ alone (8); lane 9 shows the pull-down between GST-tagged eIF2Bβ^{A286E} and eIF2Bδ^{M379E} (marked by an asterisk). Lanes 10–12 show the pull-down experiments of GST-tagged eIF2Bδ$^{130\text{-}C}$ with eIF2Bα (Lane 10), eIF2Bα and -β (11), and eIF2Bβ alone (12); lane 13 shows the pull-down between GST-tagged eIF2Bδ$^{130\text{-}C,M379E}$ and eIF2Bβ^{A286E} (marked by an asterisk). (**B**) GST pull-down analysis of the effect of point mutations on eIF2Bα$_2$ incorporation into eIF2B(βδ)$_2$ complexes. Lanes 1–3 show isolated proteins as reference. The combinations of the different mutants are indicated above the gel. (**C**) Effect of the triple mutant eIF2Bα^{T304E,P305L,I306E} on formation of eIF2Bα$_2$(βδ)$_2$ complexes. MALS analysis shows that the complex formed in the presence of eIF2Bα^{T304E,P305L,I306E} (red lines) yields a molar mass distribution (MW of 198 kDa) very similar to that of the eIF2B(βδ)$_2$ complex alone (gray lines; MW of 186 kDa) but significantly smaller than that for the wild-type complex (black lines; MW of 257 kDa). (**D**) eIF2Bα compensates the destabilization of eIF2B(βδ)$_2$ complexes by the poly-alanine mutation in eIF2Bδ. While eIF2Bα^{T304E,P305L,I306E} fails to interact with eIF2Bβ and eIF2Bδ^{PolyAla} resulting in an unstable molar mass distribution for the eIF2Bβδ^{PolyAla} complexes (green lines), wild-type eIF2Bα forms a stable eIF2Bα$_2$(βδ^{PolyAla})$_2$ complex (red lines; MW of 249 kDa) that is virtually identical to the wild-type complex (black line; MW of 257 kDa).

interactions between the other two dimers (Figure 6C and Supplementary Figure S5). Consistently, eIF2Bα$_2$ can counteract the destabilizing effect of the eIF2Bδ^{PolyAla} mutation on eIF2B(βδ)$_2$ complexes (Figure 5D), most likely through its ability to bridge both eIF2Bβδ heterodimers across the dimer-dimer interface (Figure 6C). The same effect explains the observation by Proud and coworkers that mammalian eIF2Bα stabilizes dimerization of eIF2B(βδγϵ) tetramers to form the eIF2B(αβδγϵ)$_2$ decamer (18). Moreover, the redundancy in the role of the two eIF2Bα monomers to bridge the two eIF2Bβδ dimers explains why dimerization of *hs*eIF2B(βδγϵ) occurs even after the disruption of the *hs*eIF2Bα$_2$ homodimer by exchange of V183 against Phe (18). Finally, disruption of the eIF2B(βδγϵ) tetramer by the mutation *hs*eIF2Bδ^{A391D}, which causes a severe VWM phenotype (32), is suppressed by eIF2Bα$_2$ (18). We suggest that, analogous to the eIF2Bδ^{PolyAla} mutation, eIF2Bα$_2$ compensates the destabilizing effect of the A391D mutation on canonical heterodimerization (Figure 4B) by bridging eIF2Bβ and -δ—this time however across the canonical dimerization interface (Figure 6C).

Taken together, the proposed *tk*RBPI-like arrangement of eIF2Bα$_2$(βδ)$_2$ provides a conclusive explanatory framework for available experimental data and can thus be considered as a valid structural model for eIF2B^{RSC}.

Ligand binding by eIF2Bα, -β and -δ

Sequence and structural homology between regulatory eIF2B subunits, M1PIs and RBPIs suggest a common evolutionary descent (33,34). Based on the structural work presented above, it is reasonable to assume that the eIF2B^{RSC} is derived from a *tk*RBPI-like metabolic enzyme that underwent refunctionalization during evolution to act as regulatory translation initiation factor (see Discussion). This would consequently mean that although eIF2Bα, -β and -δ most likely lost their catalytic proficiency, they might have retained the ability to bind sugar phosphates as allosteric effectors using the inter-domain cavity as binding site. Support for this idea is provided by various earlier studies in

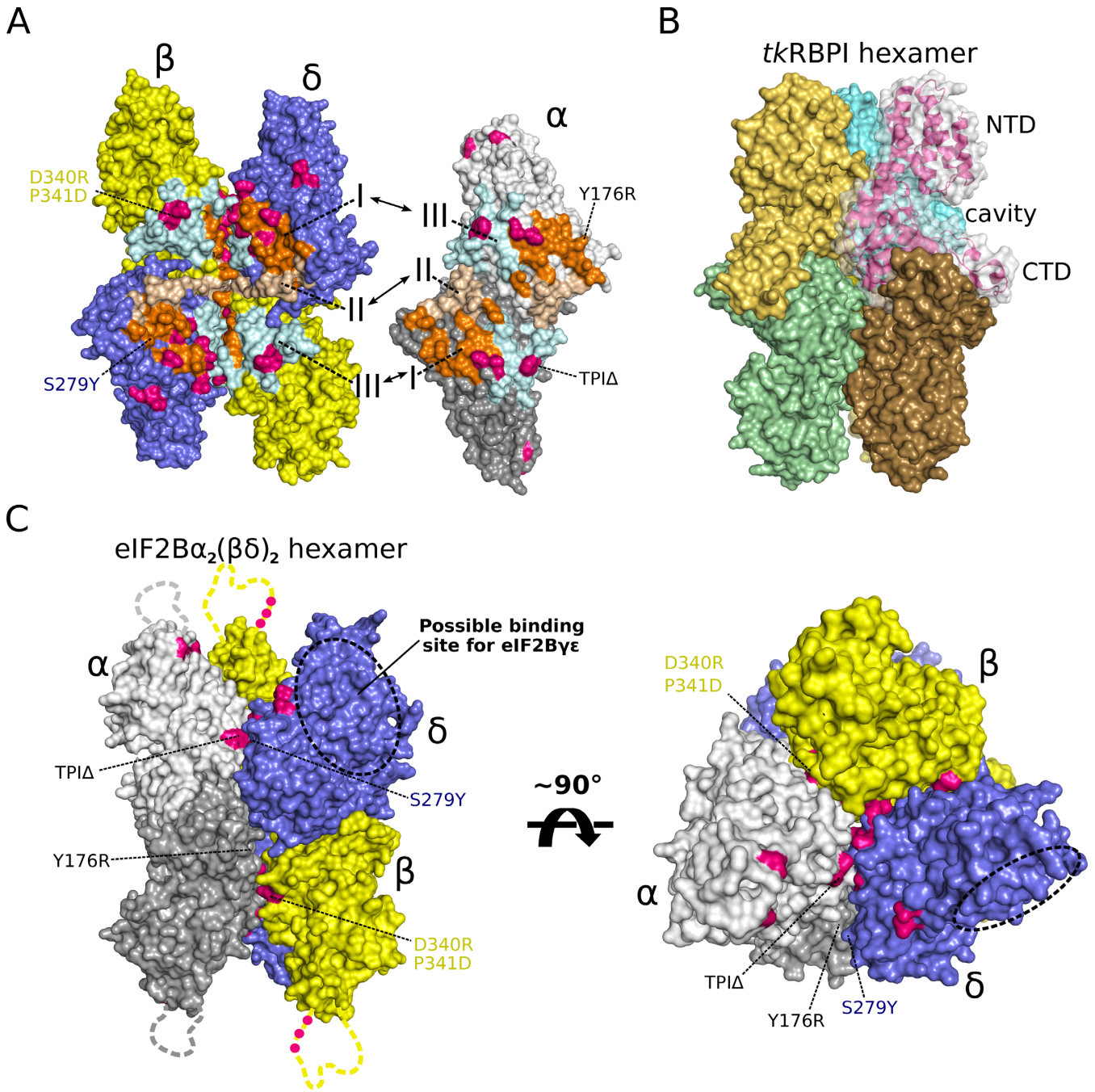

Figure 6. Structural model for the hexameric eIF2B$\alpha_2(\beta\delta)_2$ regulatory subcomplex. (**A**) Proposed interfaces for eIF2Bα_2 incorporation into the eIF2B$(\beta\delta)_2$ complex. In homology to their own dimer-dimer interface, the eIF2B$(\beta\delta)_2$ complex (left) provides a 2-fold rotation-symmetrical interface for eIF2Bα_2 (right) formed by areas I (orange surfaces), areas II (light brown surfaces), and areas III (cyan surfaces) on the C-terminal domains. The complex is formed by the association of each area I in eIF2Bα_2 with area III of eIF2Bβ and of areas II and III in eIF2Bα_2 with areas II and I in eIF2Bδ, respectively (analogous to eIF2B$(\beta\delta)_2$ formation; see also Supplementary Figure S5). The majority of identified Gcn$^-$ mutations (pink surfaces) are located in the three dimer–dimer interfaces (see also Supplementary Figure S5). The resulting eIF2B$\alpha_2(\beta\delta)_2$ regulatory subcomplex (**C**) is structurally homologous to the hexamer of *tk*RBPI (PDB 3A11) (**B**), with the three canonical dimers assembled around a pseudo 3-fold rotation axis. Mutations that destabilize or disrupt eIF2Bα_2 binding to the eIF2B$(\beta\delta)_2$ complex are indicated in (**A**) and (**C**). Dashed lines at the NTDs of eIF2Bα and -β indicate flexible loop regions that are not resolved in the crystal structures and contain additional Gcn$^-$ mutation sites (pink dots). Black dashed circles in (**C**) indicate the putative binding site for the catalytic eIF2B$\gamma\epsilon$ complex as suggested by surface conservation and VWM/CACH mutations in this area (see also Supplementary Figure S9).

which mammalian eIF2Bβ and eIF2Bδ were reported to bind GTP, ATP and $NADP^+$ (35–38).

Thermal shift analysis was initially used to identify possible ligands through their influence on the thermal stability of the three subunits (Supplementary Figure S6A–E). Surprisingly, significant stabilizing effects were only observed for the α-subunit. The strongest stabilization was mediated by AMP and GMP ($\Delta T_m = 5–7°C$). Moderate stabilizing effects ($\Delta T_m = 2–3°C$) were observed for CMP, glucose 6-phosphate (G6P) and ribose 5-phosphate (R5P), whereas ATP, GTP, $NADP^+$, phosphoenolpyruvic acid (PEP), ribulose 1,5-bisphosphate (RuBP), fructose 1,6-bisphosphate (F16BP) and dihydroxyacetone phosphate (DHAP) had no apparent influence on T_m. By contrast, eIF2Bβ was only moderately affected ($\Delta T_m \approx 2°C$) by GDP, GTP, G6P and F16BP, while eIF2Bδ remained unaffected by any of the used ligands.

In order to test whether the ligand-dependent shift in T_m was due to a specific binding to eIF2Bα, we performed ITC measurements in which the different ligands were titrated against the protein (Figure 7A and Supplementary Figure S6F) (unfortunately, ligand binding by eIF2Bβ could not be further tested by ITC due to instability of the protein). In agreement with the results from the thermal shift assays AMP as well as GMP bound eIF2Bα tightly with equilibrium dissociation constants (K_d) of 10 μM and 2.9 μM, respectively (Table 2). In both cases the binding reaction was enthalpy-driven with negative contributions for the binding enthalpy and opposing entropic contributions. Binding reactions were also observed for CMP, R5P, G6P and PO_4^{2-} albeit with significantly lower affinities. No binding signal was observed for ATP, GTP, GDP, $NADP^+$, RuBP and DHAP in agreement with the absence of any effect on T_m.

These results demonstrated that *ct*eIF2Bα interacts specifically with sugar monophosphates with an apparently strong preference for mono-phosphorylated purine nucleosides (AMP and GMP). A critical question that arose from this observation was whether eIF2Bα—like *tk*RBPI—uses the inter-domain cavity as ligand binding site. We therefore generated two point mutants for the putative binding site, *ct*eIF2Bα^{E260K} and *ct*eIF2Bα^{S270Y}, which correspond to the Gcd^- mutation E199K in *sc*eIF2Bα and the VWM mutation N208Y in *hs*eIF2Bα, respectively. Both positions are well conserved among eIF2Bα homologs (Supplementary Figures S3) and correspond to D202 and N212 in *tk*RBPI—residues that are directly involved in interactions with the substrate ribose 1,5-bisphosphate (31). According to ITC experiments and thermal shift analysis, these mutations completely abolished the interactions with any of the previously identified ligands (Figure 7A and Supplementary Figure S6C). Our results thus provide strong evidence for the homology between the ligand binding sites in eIF2Bα and *tk*RBPI (Figure 7B). Importantly, both mutants formed stable complexes with eIF2B$(\beta\delta)_2$ in pull-down experiments, indicating correct tertiary structures (Figure 5B, Lanes 12 and 13).

DISCUSSION

The eIF2B^{RSC} is a homolog of the hexameric *tk*RBPI

Our results consistently demonstrate that the eIF2B^{RSC} from *C. thermophilum*, comprising the homologous subunits eIF2Bα, -β and -δ, is structurally closely related to the homohexameric ribose 1,5-bisphosphate isomerase from the archaeon *T. kodakarensis*. We show that the eIF2B^{RSC} exists as a stable $\alpha_2(\beta\delta)_2$ hexamer in solution composed of two canonical eIF2Bβδ heterodimers and one canonical eIF2Bα_2 homodimer that assemble coaxially around a pseudo 3-fold rotation axis (Figure 6). Each of the three dimers is bound by a composite interface provided by the other two dimers, resulting in an extensive network of mutually stabilizing interactions. All interfaces are thereby formed by three well conserved regions (termed areas I, II and III) at the homologous backsides of the six C-terminal RFL domains clustering around the N-terminus of helix α12. As a consequence, the inter-domain cavity of each monomer is oriented outwards, facing the solvent side of the complex. The six all α-helical NTDs point away from the center of the hexamer and form two sets of three axially arranged NTDs on opposite sides of the complex with each set containing the NTDs from one α-, one β- and one δ-subunit.

This *tk*RBPI-like architecture of the eIF2B^{RSC} is in excellent agreement with the recent finding that yeast and human eIF2B form stable decameric complexes comprising two copies of each of the five subunits (17,18). The core of this decamer appears to be formed by the two eIF2Bβδ dimers, which form the platform for the association of eIF2Bα_2 as well as of two eIF2Bγε catalytic subcomplexes. The question where and how the catalytic subcomplexes bind to the eIF2B^{RSC} cannot be unambiguously answered on the basis of the available data. MS analysis suggest a critical role for eIF2Bδ in the formation of *hs*eIF2Bβδγε complexes, indicating that the δ-subunit provides the primary binding site for the left-handed β-helix (LβH) domains of eIF2Bγ and -ε with possible additional contributions by the β-subunit (18). Notably, Marintchev and coworkers observed that a subset of surface-exposed VWM/CACH mutations that reduce eIF2B activity maps to a region in the eIF2Bδ-NTD whose relatively high degree of sequence conservation and surface hydrophobicity are idiosyncratic to this subunit (21) (Supplementary Figure S9B/C). According to our eIF2B$\alpha_2(\beta\delta)_2$ model this region faces the solvent side of the hexameric assembly and may thus provide two binding sites for the eIF2Bγε subcomplexes on opposite sides of the eIF2B^{RSC} (Figure 6C). On this basis we propose that decamer-formation in eIF2B is primarily mediated by the eIF2B$(\beta\delta)_2$ tetramer, with eIF2Bα_2 merely playing a stabilizing role by bridging between the two eIF2Bβδγε tetramers (Figure 6 and Supplementary Figure S5). This is in line with the fact that eIF2Bα can be readily lost from eIF2B complexes without negatively affecting the association between eIF2Bβδ and eIF2Bγε complexes (17,18). It is important to note however that while the loss of eIF2Bα results in stable eIF2B$(\beta\delta)_2(\gamma\epsilon)_2$ complexes in yeast eIF2B (17), its loss from mammalian eIF2B appears to cause dissociation of the two eIF2Bβδγε tetramers, indicating a less

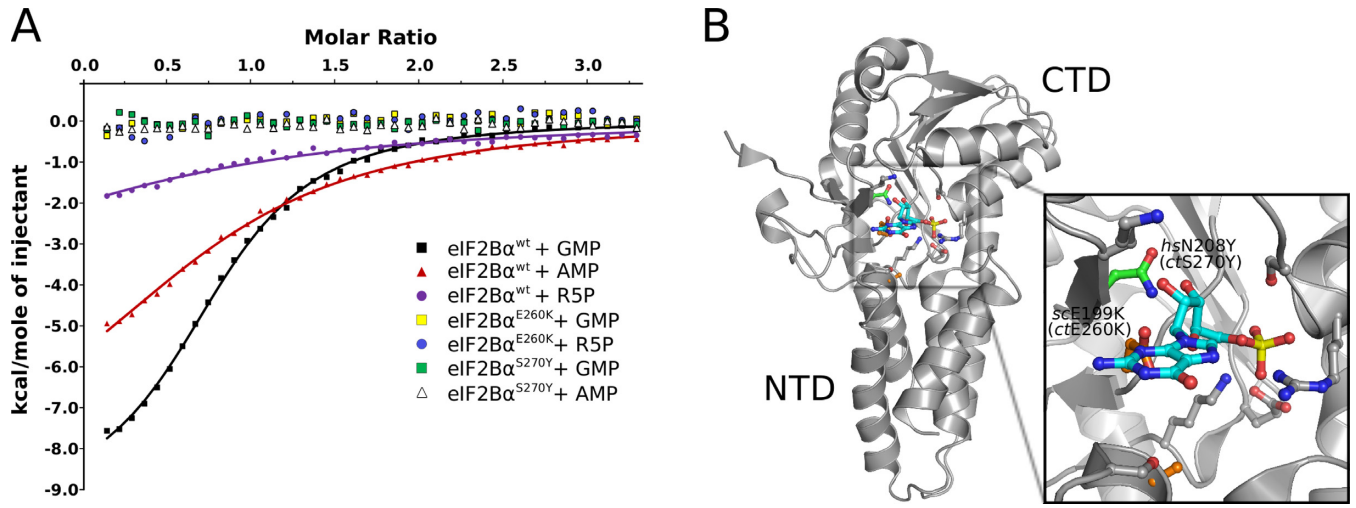

Figure 7. Ligand binding by eIF2Bα. (**A**) ITC experiments for the binding of pentose phosphate ligands by *ct*eIF2Bα. Wild-type *ct*eIF2Bα binds tightly to GMP (black squares) and AMP (red triangles) and moderately to ribose 5-phosphate (R5P; purple circle). The binding reaction to either ligand is entirely lost in the inter-domain cavity mutants eIF2Bα^{E260K} and eIF2Bα^{S270Y} (see also Supplementary Figure S6). (**B**) Structure of *hs*eIF2Bα (PDB 3ECS) with GMP modeled into the proposed ligand binding site of the inter-domain cavity (inset). Conserved residues that are likely to be involved in ligand binding are indicated as sticks. The *ct*E260K mutation corresponds to the Gcd$^-$ mutation *sc*E199K (orange sticks), the *ct*S270Y mutation corresponds to the VWM mutation *hs*N208Y (green sticks). The GMP molecule was modeled according to the position of the sulfate ion in the crystal structure of *hs*eIF2Bα and of the R15BP substrate bound to *tk*RBPI (PDB 3VM6) (see also Supplementary Figure S7A).

Table 2. Thermodynamic parameters of *ct*eIF2Bα binding to various ligands

Ligand	ΔT_m [°C]	K_d [μM]	ΔH [*kcal/mol*]	ΔG [*kcal/mol*]	$T\Delta S$ [*kcal/mol*]
GMP	+7	2.9	−9.4	−4.9	−1.3
AMP	+5	10	−8.6	−4.4	−1.2
R5P	+3	24	−4.8	−4.1	0.9
CMP	+2	65	−8.4	−3.7	−1.8

ITC measurements were performed two times (at 20°C).
ΔT_m, change in melting temperature according to thermal shift analysis.
K_d, equilibrium dissociation constant; calculated as $1/K_a$.
K_a, equilibrium association constant; standard deviation did not exceed ±15%.
ΔH, standard enthalpy change; standard deviation did not exceed ±15%.
ΔG, Gibbs energy; calculated from equation $\Delta G = -R \cdot T \cdot \ln K_a$.
$T\Delta S$, standard entropy change; calculated from equation $\Delta G = \Delta H - T\Delta S$.

stable association between the two eIF2Bβδ dimers (18). As suggested by Proud and coworkers, this feature may have evolved in mammals as an additional level of tissue-specific regulation of eIF2B activity based on varying ratios between eIF2B$(\alpha\beta\gamma\delta\epsilon)_2$ and eIF2Bβγδε complexes as regulated by the expression levels of the α-subunit (18), which would not be required in the ascomycetes *S. cerevisiae* or *C. thermophilum*. Taken together, the proposed architecture for the eIF2Bα$_2$(βδ)$_2$ subcomplex provides a consistent framework to explain the respective pivotal roles of eIF2Bβδ and eIF2Bα$_2$ for the formation of eIF2B$(\alpha\beta\delta\gamma\epsilon)_2$ complexes from eIF2Bβδγε tetramers. In this context, it is also important to note that the central role for the eIF2B$(\beta\delta)_2$ complex provides an explanation for the large number of VWM/CACH mutations that map to the canonical dimerization interface between eIF2Bβ and -δ and thus most likely undermine the integrity of the entire eIF2B complex (Supplementary Figure S9C; see also (21)).

Model for nonproductive binding of eIF2(α-P) by eIF2B^{RSC}

A key question that arises from the proposed architecture for eIF2B^{RSC} regards the binding sites for eIF2 or eIF2(α-P). Previous evidence points toward a scenario in which the regulatory subcomplex provides two mutually exclusive binding sites for eIF2α (9,13). On the one hand, the non-productive binding site for eIF2 prevents nucleotide exchange on eIF2γ by eIF2Bε; this binding mode depends on contributions by all three regulatory subunits and is stabilized by eIF2α phosphorylation. The productive mode of eIF2 binding on the other hand is permissive for or even promotes nucleotide exchange on eIF2γ by eIF2Bε and is mediated by a surface which is particularly dependent on eIF2Bβ (13). Thus, the two binding sites are not necessarily overlapping, but occupation of the first site by eIF2(α-P) prevents binding of eIF2 to the second.

Extensive genetic and biochemical studies demonstrated that the majority of mutations that render eIF2B insensitive to inhibition by eIF2(α-P) and thus confer a Gcn$^-$ phenotype map to homologous evolutionarily well conserved surfaces on the CTDs of all three regulatory subunits (Sup-

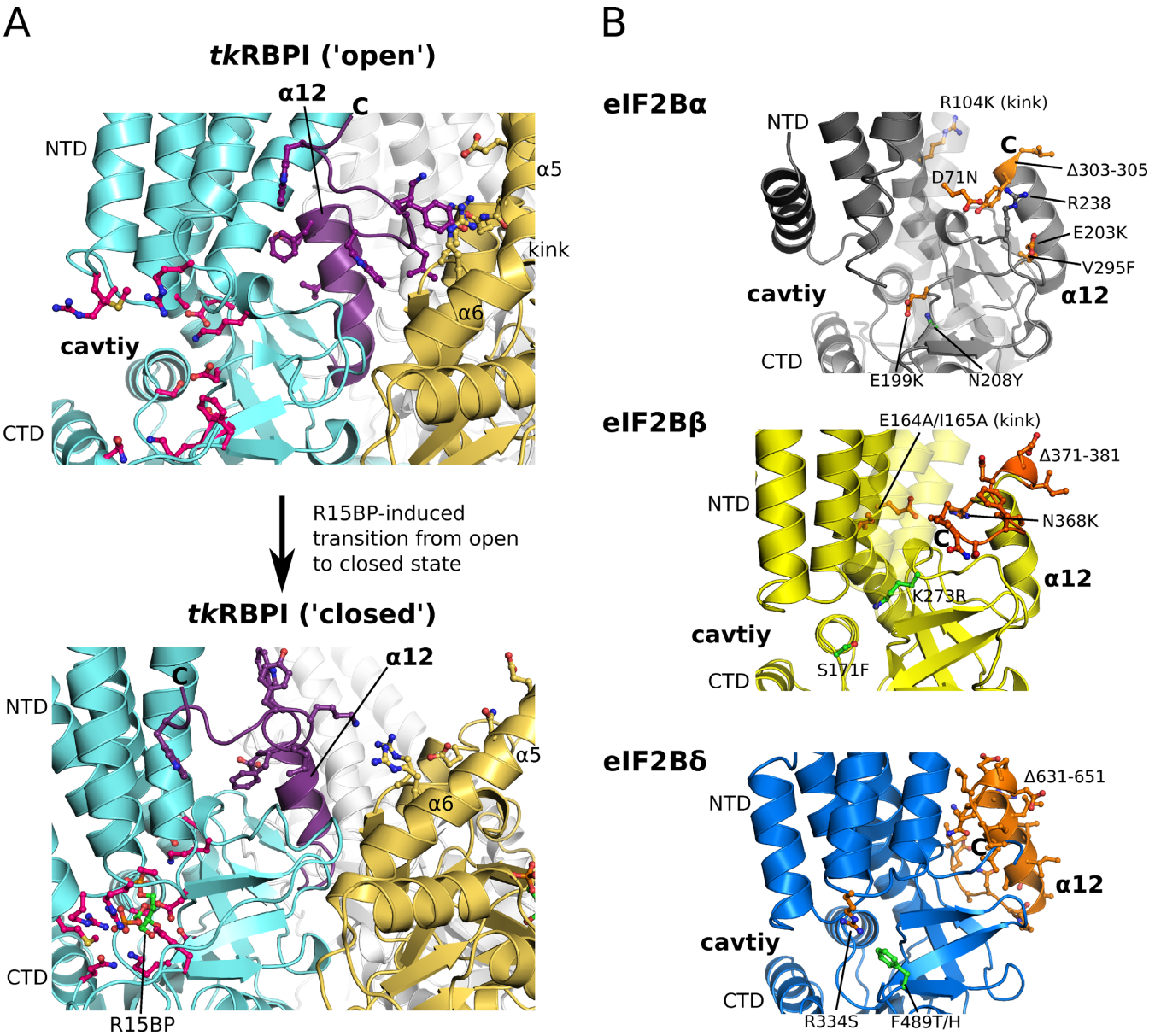

Figure 8. Gcd$^-$ and VWM/CACH mutations and their implications for the conformational transition between an open and closed state in eIF2Bα/β/δ. (**A**) Conformational transition in *tk*RBPI between the 'open' apo state (upper panel; PDB 3A11) and the 'closed' substrate-bound state (lower panel; PDB 3VM6) in one monomer (cyan) in the context of the hexamer. Regions stabilizing the open conformation are the C-terminus of helix α12 (purple) which forms a direct contact to the NTD, as well as the C-terminal peptide which interacts with residues in the kink region of helices α5 and α6 in the adjacent *tk*RBPI monomer (yellow). Transition to the 'closed' state is induced by binding of the substrate ribose 1,5-bisphosphate (R15BP) in the inter-domain cavity (R15BP binding residues are shown as pink sticks). Simultaneously, the NTD undergoes a ∼25° rotation outward, accompanied by the loss of direct interactions with helix α12 and the C-terminal peptide of the adjacent monomer (see also Supplementary Figure S7A). (**B**) Positions of Gcd$^-$ (orange; *S. cerevisiae* numbering) and VWM/CACH mutations (green; *H. sapiens* numbering) in eIF2Bα (upper panel), eIF2Bβ (middle) and eIF2Bδ (lower panel). The orientation of the subunits is the same as that of the cyan *tk*RBPI monomer in (**A**). Helix α12 in eIF2Bδ was modeled as shown in Figure 2C. Gcd$^-$ and VWM/CACH mutations cluster in regions involved in the conformational transition in *tk*RBPI shown in (**A**). This includes the inter-domain cavity (see also Supplementary Figure S7B), helix α12, the C-terminal peptide (Δ371–381 in *sc*eIF2Bβ), and the kink region in α5/α6 (R104K in *sc*eIF2Bα and E164A/I165A in *sc*eIF2Bβ).

plementary Figures S8 and S9). Based on this evidence it was suggested that these surfaces may be aligned in the regulatory subcomplex to form a composite binding site for eIF2(α-P) (21,34). However, our own work demonstrates that these regions in fact form the extensive surface areas used for dimer-dimer association within the eIF2B$\alpha_2(\beta\delta)_2$ complex (Figures 4A, 6A and Supplementary Figure S5). This implies that most if not all of these residues altered by Gcn$^-$ mutations are involved in inter-dimer contacts and contribute to the stability of the eIF2B^{RSC}. This is corroborated by the loss of eIF2Bα_2 from the eIF2B^{RSC} due to the mutants *ct*eIF2B$\alpha^{T304E,P305L,I306E}$ (*ct*T304E corresponds to the Gcn$^-$ mutation *sc*F240L/I) and *ct*eIF2B$\beta^{D340R,P341E}$

(corresponding to Gcn⁻ mutations *sc*Y305C and *sc*P306L) (Figures 5 and 6).

Importantly, a small subset of Gcn⁻ mutations lies outside of the three dimer-interfaces and maps to the outward-pointing tips of the N-terminal helix bundles in eIF2Bα and eIF2Bβ (Figure 6C, Supplementary Figures S8D and S9D). All six positions lie in the flexible loop regions between α-helices and have no apparent effect on the structural integrity of the individual subunits or on inter-dimer contacts (most of these Gcn⁻ sites are not resolved in the crystal structures) (Figure 6). We propose that the non-productive binding site for the S1 domain of eIF2(α-P) is provided by the tips of the three axially arranged NTDs (one αβδ-NTD heterotrimer on each side of the hexamer), involving direct contacts to those six residues that are altered by Gcn⁻ mutations in eIF2Bα and -β (T41 (*hs*T41), E44 (*hs*G44), N80 (*hs*A79) in *sc*eIF2Bα and L117 (*ct*V148), I118 (*ct*S149), S119 (*ct*K150) in *sc*eIF2Bβ). In contrast to previous assumptions, this implies that only the Gcn⁻ mutations in the NTDs confer their effect on eIF2(α-P) binding directly, whereas all other Gcn⁻ mutations affect nonproductive eIF2(α-P) binding indirectly by disrupting the two heterotrimers of αβδ-NTDs on both sides of the regulatory complex, e.g. by expelling eIF2Bα$_2$ from the eIF2Bα$_2$(βδ)$_2$ hexamer.

This scenario for eIF2(α-P) binding provides a rationale for the molecular effects of Gcn⁻ mutants. It is consistent with the fact that eIF2(α-P) binding depends on functionally related contributions by all three subunits (9,13) and explains how sensitivity to eIF2α phosphorylation is lost due to the absence of eIF2Bα (39) caused by Gcn⁻ mutations that destabilize its association with the eIF2B^{RSC} (Figures 5 and 6).

Conformational changes in eIF2Bα$_2$(βδ)$_2$ might regulate its interactions with eIF2

Interestingly, the above model for eIF2(α-P) binding suggests a tempting scenario for the mechanism by which eIF2B^{RSC} discriminates between eIF2 as substrate and eIF2(α-P) as competitive inhibitor; a scenario that is based on the assumption that the observed structural homology between eIF2B and *tk*RBPI (Figure 6B/C) is a true homology based on common evolutionary descent and not merely the result of convergent evolution (see also below).

Nakamura *et al.* demonstrated that the catalytic activity of the *tk*RBPI complex depends on a concerted conformational transition of its monomers between an 'open' apo/product-bound form (characterized by a strong kink between helices α5/α6 and an open inter-domain cavity) and a 'closed' substrate-bound state (characterized by a reduced α5/α6 kink and a closed inter-domain cavity) (31) (Supplementary Figure S7A). In each monomer, the transition from the open to the closed state involves a ∼25° rotation of the NTD with respect to the C-terminal RFL domain accompanied by the loss of stabilizing contacts between helix α12 and the NTD (Figure 8A). In the structural context of the hexamer, the simultaneous transition of all monomers causes the tips of the three NTDs to move apart by ∼23 Å (from ∼20 to ∼43 Å), thereby breaking also the indirect contacts between the NTDs mediated by the peptide C-terminal to helix α12 and the α5/α6-kink region of the adjacent monomer (Figure 8A). During this transition, the core of the complex—formed by the six RFL domains—remains essentially unchanged (Supplementary Figure S7A).

Given the hypothesis that the non-productive binding site for eIF2(α-P) is formed by the tips of the three NTDs on both sides of the eIF2B^{RSC} (see above), whereas productive binding is primarily mediated by eIF2Bβ alone (13), a conformational transition in the regulatory subcomplex analogous to that in *tk*RBPI would necessarily affect its propensity to interact either productively or non-productively with eIF2 or eIF2(α-P). eIF2(α-P) might thus act as competitive inhibitor for unphosphorylated eIF2 not by competing for the same binding site on eIF2B, but instead by stabilizing a conformation of the NTDs that is incompatible with the productive mode of eIF2 binding (Figure 9). This hypothesis results in a necessary conclusion: Mutations in regulatory subunits that affect the relative orientation between N- and C-terminal domains and favor either a closed or an open conformation should change the equilibrium between the two alternative conformational states of the eIF2B^{RSC}, thereby promoting either the productive or non-productive mode of eIF2 binding. Importantly, this prediction is in good agreement with previous evidence for a number of Gcd⁻ mutations in yeast eIF2Bα dubbed *gcn3^c* alleles (D71N, R104K and E199K) (12), and eIF2Bβ (E164A/I165A, N368K and Δ371–381) that were reported to mimic the effect of eIF2(α-P) by conferring tighter non-productive binding of unphosphorylated eIF2 (13,14); an effect that is suppressed by the Gcn⁻ mutation L84F in eIF2α which specifically overcomes the inhibitory effect of eIF2α phosphorylation (14). Without exception, all these mutations map to regions that play critical roles in the assumed conformational transition between the two alternative states of the regulatory subcomplex by specifically stabilizing the open conformation within the individual subunits and/or by stabilizing interactions between adjacent NTDs in the hexamer with its subunits in the open state (Figure 8). We therefore suggest that most Gcd⁻ mutants destabilize the open conformation of the regulatory subcomplex (with NTDs close together) and thereby on the one hand disrupt the productive binding site for eIF2 while at the same time shifting the equilibrium toward the non-productive mode (Figure 9), thus bypassing the requirement for eIF2α phosphorylation for tight binding (13). A similar explanation may also account for the lethality of the *sc*eIF2Bβ^{T262A,K263A} double mutant which reduces productive binding of eIF2 (13). Instead, Gcd⁻ mutations that disrupt proper folding or remove helix α12 entirely (e.g. Δ303–305 and V295F in *sc*eIF2Bα, Δ631–651 in *sc*eIF2Bδ) are likely to mediate their effect by destabilization of the entire eIF2B complex, which could explain why they are not suppressible by eIF2α^{L84F} (13,14). According to our hypothesis the only Gcd⁻ mutation that would confer its effect by increasing eIF2(α-P) binding to eIF2B directly is *sc*eIF2Bα^{H82Y} (*hs*L81). Like the six Gcn⁻ mutations that we proposed to destabilize eIF2(α-P) binding directly (see above), *hs*L81 is located in a flexible loop at the tip of the NTD, which we assume to form the binding site for eIF2(α-P) (Figure 9 and Supplementary Figure S8C). It is finally

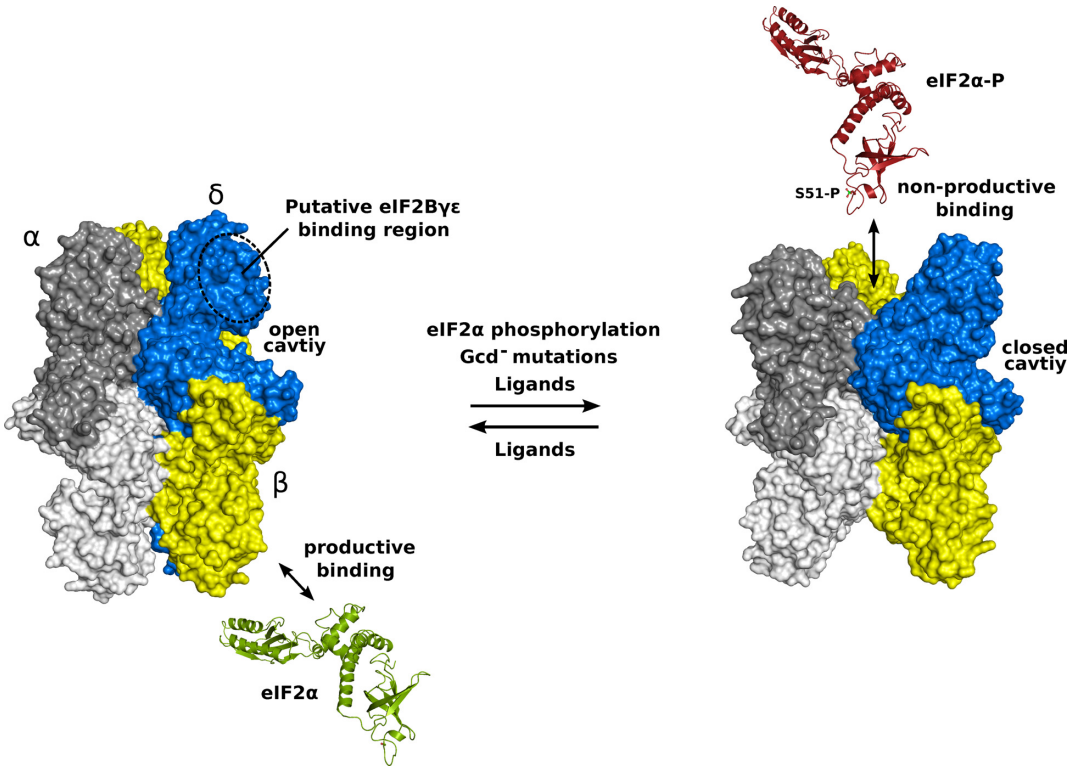

Figure 9. Model for the interactions between the eIF2B regulatory subcomplex and eIF2α. According to the model, hexameric eIF2B$\alpha_2(\beta\delta)_2$ exists in an equilibrium between two alternative conformational states: in one conformation the individual monomers adopt an open state, thereby placing the NTDs of the two heterotrimers close together (left panel). In the second conformation, the individual monomers adopt the closed state with their NTDs far apart from each other (right panel). The open form of the hexamer provides the interaction surfaces for the productive binding of unphosphorylated eIF2 (green cartoon), most likely involving eIF2Bβ. The productive binding site is disrupted in the closed conformation, which instead allows non-productive binding of eIF2α presumably between the tips of the NTDs as suggested by a number of Gcn^- mutations in this region (Figure 6C, Supplementary Figures S8D and S9D). Due to a higher affinity of eIF2(α-P) for the non-productive binding site, the presence of eIF2α-P (red cartoon) shifts the equilibrium between the two states toward the right, thereby acting as competitive inhibitor for productive eIF2 binding. Likewise, Gcd^- mutations that destabilize the open state (Figure 8) shift the equilibrium to the right, thereby bypassing the requirement for S51-P in eIF2α for stable non-productive binding of eIF2. A third possibility to shift the equilibrium in either direction is the allosteric effect of ligands (e.g. AMP, GMP, ATP, GTP, $NADP^+$ and other sugar phosphates) that bind to the inter-domain cavity and thereby stabilize either the open or closed state. A possible binding site for the catalytic eIF2Bγε complex is indicated in the left panel on the basis of the two VWM/CACH mutations that map to this region of the eIF2Bδ-NTD (see also Supplementary Figure S9C). The two structural models are based on the crystal structures of apo and R15BP-bound *tk*RBPI (PDBs 3A11 and 3VM6).

important to note that the proposed conformational transition between productive and non-productive conformations of the $eIF2B^{RSC}$ does not necessarily require a concerted movement of all three NTDs as shown in Figure 9. In fact the rearrangements could be smaller and limited to one or two of the three subunits, which could still be sufficient to remodel the proposed binding sites and thus alter the specificity of eIF2B for eIF2 or eIF2(α-P).

Evolution of eIF2B and its implications for the origin of its regulation by eIF2α

Translation is one of the most fundamental cellular processes and highly conserved between bacteria, archaea and eukarya. Yet, the initiation phase of translation, although conserved in its basic componentry and underlying principles, incurred a massive divergence in the three domains of life, in particular with regard to the number and complexity of the essential auxiliary initiation factors (40,41). Due to this complexity, the reconstruction of the origins of the derived archaeal and eukaryal features of translation initiation constitutes a major challenge which not only provides clues as to the nature of the primary branchings on the phylogenetic tree but may have direct implications for the intricate mechanisms in extant organisms. The eukarya-specific initiation factor eIF2B, with its unusual complexity, its involvement in the nucleotide cycle of eIF2 as multifunctional GEF as well as its intricate regulation mechanisms within the context of the ISR, constitutes an interesting example in this regard. As for all biological systems, the challenge is to understand the structure of the extant eIF2B complex and its interactions with eIF2 as the result of a historical process of slow adaptive changes under contingent and constantly changing contexts, emerged from a likewise historical and contingent origin.

Based on sequence analysis (34), the structures of the individual eIF2Bα, -β and -δ subunits (Figures 2 and 4) as well as the reconstruction of the qaternary $eIF2B^{RSC}$ structure (Figures 4A, 6 and Supplementary Figure S5) we suggest that the $eIF2B^{RSC}$ evolved from a homohexameric *tk*RBPI-like enzyme involved in sugar phosphate metabolism. Either in the common ancestor of archaea and eukarya or early in the eukaryal lineage, this ancestral

*tk*RBPI-like enzyme complex must by chance have acquired the ability to interact with the S1 domain of the α-subunit in a/eIF2. Due to a dependency of these early interactions on the allosterically regulated, ligand-induced conformational changes within the ancestral hexamer (Supplementary Figure S7A), these interactions may have conferred a selective advantage by the opportunity to sequester a/eIF2 and thus regulate translation rates in direct response to the energy state of the cell, thus becoming an object to selective pressure. As a consequence, the subsequent development of the ancestral eIF2B^{RSC} would have been characterized by a refinement of the ligand-dependent regulation of its interactions with a/eIF2α. This includes the two consecutive gene-duplication events that eventually gave rise to the three regulatory subunits eIF2Bα, -β and -δ, which may have allowed the ancestral eIF2B^{RSC} to respond to a broader spectrum of allosteric effectors. Thus, as typical for evolutionary processes that are characterized by the function-independent carry-over of structural and mechanistic features from an ancestral to a new mechanistic context, an originally secondary effect of the (primary) enzymatic activity, namely the substrate-induced conformational rearrangements, acquired the primary role of regulation of its interactions with a/eIF2α (Figure 9). This refunctionalization of the ancestral eIF2B^{RSC} complex from a metabolic enzyme to a regulatory translation initiation factor would then have been accompanied by the loss of catalytic proficiency, while it retained the ability to bind metabolic intermediates as allosteric regulators and thus to act as metabolic sensor that correlates translation rates with the energy state of the cell.

Notably, this scenario is supported by empirical evidence (34). Sequence analysis revealed the existence of a distinct phylogenetic group of archaeal eIF2B-like proteins (aIF2Bs) of unknown function that specifically groups with eIF2Bα/β/δ (34). Like eIF2Bα/β/δ aIF2Bs have lost the majority of catalytic residues found in M1PIs and RBPIs (34). Instead, aIF2Bs specifically interact with their cognate aIF2α and even with yeast eIF2α in a manner depending on its S1 domain (34). This interaction was found to be independent of phosphorylation of a/eIF2α, in line with the fact that the critical Ser51 is not conserved among aIF2α homologs. Based on this evidence, it was proposed that aIF2Bs may constitute archaeal orthologs of eIF2Bα/β/δ that play a role in the regulation of nucleotide exchange on aIF2 (34). Although the physiological role of these interactions is not clear at present, this interpretation is in line with our proposal of a phosphorylation-independent origin for the eIF2B^{RSC}-eIF2α interaction in a common ancestor of archaea and eukarya that antedates the occurrence of the catalytic role of eIF2B as GEF. In this context, it is interesting to note that the same study reported the co-purification of a sugar-phosphate nucleotidyltransferase with aIF2B from *T. kodakarensis* which shares sequence and structural similarity with eIF2Bγ and -ϵ but lacks the catalytic W2 domain of eIF2Bϵ (34). This suggests that the eIF2Bγϵ catalytic subcomplex—similar to eIF2B^{RSC}—may have evolved from an enzyme involved in nucleotide sugar metabolism, which acquired the GEF function later by the attachment of the genetically mobile ∼20 kDa W2 domain at the C-terminus of eIF2Bϵ (42–44). The association between regulatory and catalytic subcomplexes within eIF2B could thus be inherited as the result of a functional interaction between their respective ancestral enzyme complexes.

Importantly, the reconstruction of the evolutionary history of eIF2B^{RSC} results in specific implications for the regulation of extant eIF2B. According to our interpretation, the intricate eIF2(α-P) dependent regulation mechanism of eIF2B in the context of the ISR originates from the phosphorylation-independent regulation of the eIF2B^{RSC}–eIF2α interactions by allosteric effector molecules. Hence, although the ISR may dominate the regulation of eIF2B, an underlying mechanism of direct phosphorylation-independent regulation by metabolic intermediates may still exist today. This results in the prediction that eIF2B^{RSC} subunits still bind ligands as allosteric effectors. In line with this prediction, we demonstrated that *ct*eIF2Bα interacts specifically with a number of nucleotide sugar phosphates (Figure 7 and Supplementary Figuer S6; Table 2). The binding reaction is mediated by the same highly conserved binding pocket in the inter-domain cavity used by *tk*RBPI to bind ribose 1,5-bisphosphate (Figure 7 and Supplementary Figure S7B). We found strong binding with low μM affinity for GMP and AMP, while less efficient binding was found for CMP, ribose 5-phosphate and phosphate ions. Notably, no binding was found for ATP, GTP and GDP. Thus, in line with the scenario for an evolutionary origin of eIF2B^{RSC} in a *tk*RBPI-like enzyme, eIF2Bα retained its ability to bind sugar phosphate ligands with a strong preference for GMP and AMP. Although it is conceivable that the ribose 5′-phosphate moiety of both nucleotides is bound in the same way as observed for R15BP in *tk*RBPI (Figure 7B and Supplementary Figure S7B), it remains to be elucidated how the purine base contributes to this specificity. In light of our structural and functional model for the eIF2B^{RSC}, we suggest that the low energy metabolites GMP and AMP, just like R15BP in *tk*RBPI, stabilize the closed conformation of eIF2Bα, thereby allosterically regulating the interaction between eIF2B^{RSC} and eIF2α in a phosphorylation-independent manner—in analogy to Gcd^{-} mutations that destabilize the open conformation (Figures 8 and 9). As we assume that the closed conformation of eIF2B subunits promotes nonproductive binding of eIF2 (Figure 9), an increase of the intracellular AMP and GMP concentrations as the result of starvation conditions (45) would consequently down-regulate translation initiation without the need for eIF2α phosphorylation. Although we could not unambiguously identify potential binding partners for eIF2Bβ and -δ (eIF2Bβ was slightly stabilized by ATP, GTP, GDP and glucose 6-phosphate (Supplementary Figure S6D/E)), earlier studies reported specific GTP binding by eIF2Bβ as well as ATP and NADP^{+} binding by eIF2Bδ (35–38). NADP^{+}/NAD^{+} was reported to inhibit the GEF activity of eIF2B (35–38), while glucose 6-phosphate and—to a lesser extend—fructose 1,6-bisphosphate stimulate the GEF activity of mammalian eIF2B (46). We hypothesize that these effects reflect different ligand specificities of the three regulatory subunits and the ability of different ligands to stabilize either the productive or non-productive conformation of eIF2B. The potentially physiologically relevant role of these interactions is underscored by the high degree of conservation of the inter-domain cavity in all three regula-

tory subunits as well as by the large number of Gcd$^-$ and VWM/CACH mutations in residues that are implicated in ligand binding in *tk*RBPI and eIF2Bα (Figure 7 and Supplementary Figure S7).

Taken together, the available data support a metabolic origin of the eIF2B^{RSC}. Our model provides a conclusive explanation for the complexity of eIF2B^{RSC} as the result of its evolutionary descent from a *tk*RBPI-like enzyme. It suggests that eIF2B evolved as metabolic sensor that used allosterically induced conformational rearrangements to modulate its interactions with eIF2 in response to stress conditions. This finally results in the conclusion that underneath the intricate mechanism of the extant ISR an underlying mechanism of allosteric regulation of eIF2B by effector molecules, bearing the characteristics of its ancient origins, may still provide the means to fine-tune the rate of translation by its direct correlation with central metabolic pathways and thus with the energy state of the cell.

ACCESSION NUMBERS

Coordinates have been deposited in the RCSB Protein Data Bank (PDB): *ct*eIF2Bβ$^{\Delta 123–148}$ (4ZEM); *ct*eIF2Bδ$^{148–443}$ (4ZEO); eIF2B$(\beta\delta)_2$ (5DBO).

SUPPLEMENTARY DATA

Supplementary Data are available at NAR Online.

ACKNOWLEDGEMENT

We thank the beam line scientists at BESSY (Berlin) as well as P. Neumann for support during X-ray diffraction data collection and M. Franke for technical assistance. Moreover, we are grateful to O. Valerius for the Mass Spectrometry analysis of protein samples as well as L. K. Dörfel for critical reading of the manuscript.

FUNDING

We acknowledge support by the German Research Foundation and the Open Access Publication Funds of the Göttingen University.
Conflict of interest statement. None declared.

REFERENCES

1. Hinnebusch,A.G. and Lorsch,J.R. (2012) The mechanism of eukaryotic translation initiation: new insights and challenges. *Cold Spring Harb. Perspect. Biol.*, **4**, a011544.
2. Hinnebusch,A.G. (2014) The scanning mechanism of eukaryotic translation initiation. *Annu. Rev. Biochem.*, **83**, 779–812.
3. Pavitt,G.D., Ramaiah,K.V., Kimball,S.R. and Hinnebusch,A.G. (1998) eIF2 independently binds two distinct eIF2B subcomplexes that catalyze and regulate guanine-nucleotide exchange. *Genes Dev.*, **12**, 514–526.
4. Jennings,M.D. and Pavitt,G.D. (2014) A new function and complexity for protein translation initiation factor eIF2B. *Cell Cycle*, **13**, 2660–2665.
5. Pavitt,G.D. (2005) eIF2B, a mediator of general and gene-specific translational control. *Biochem. Soc. Trans.*, **33**, 1487–1492.
6. Hinnebusch,A.G. (2005) Translational regulation of GCN4 and the general amino acid control of yeast. *Annu. Rev. Microbiol.*, **59**, 407–450.
7. Hinnebusch,A.G. (1993) Gene-specific translational control of the yeast GCN4 gene by phosphorylation of eukaryotic initiation factor 2. *Mol. Microbiol.*, **10**, 215–223.
8. Sonenberg,N. and Hinnebusch,A.G. (2009) Regulation of translation initiation in eukaryotes: mechanisms and biological targets. *Cell*, **136**, 731–745.
9. Krishnamoorthy,T., Pavitt,G.D., Zhang,F., Dever,T.E. and Hinnebusch,A.G. (2001) Tight binding of the phosphorylated alpha subunit of initiation factor 2 (eIF2alpha) to the regulatory subunits of guanine nucleotide exchange factor eIF2B is required for inhibition of translation initiation. *Mol. Cell. Biol.*, **21**, 5018–5030.
10. Sudhakar,A., Ramachandran,A., Ghosh,S., Hasnain,S.E., Kaufman,R.J. and Ramaiah,K.V. (2000) Phosphorylation of serine 51 in initiation factor 2 alpha (eIF2 alpha) promotes complex formation between eIF2 alpha(P) and eIF2B and causes inhibition in the guanine nucleotide exchange activity of eIF2B. *Biochemistry*, **39**, 12929–12938.
11. Pavitt,G.D., Yang,W. and Hinnebusch,A.G. (1997) Homologous segments in three subunits of the guanine nucleotide exchange factor eIF2B mediate translational regulation by phosphorylation of eIF2. *Mol. Cell. Biol.*, **17**, 1298–1313.
12. Hannig,E.M., Williams,N.P., Wek,R.C. and Hinnebusch,A.G. (1990) The translational activator GCN3 functions downstream from GCN1 and GCN2 in the regulatory pathway that couples GCN4 expression to amino acid availability in Saccharomyces cerevisiae. *Genetics*, **126**, 549–562.
13. Dev,K., Qiu,H., Dong,J., Zhang,F., Barthlme,D. and Hinnebusch,A.G. (2010) The beta/Gcd7 subunit of eukaryotic translation initiation factor 2B (eIF2B), a guanine nucleotide exchange factor, is crucial for binding eIF2 in vivo. *Mol. Cell. Biol.*, **30**, 5218–5233.
14. Vazquez de Aldana,C.R. and Hinnebusch,A.G. (1994) Mutations in the GCD7 subunit of yeast guanine nucleotide exchange factor eIF-2B overcome the inhibitory effects of phosphorylated eIF-2 on translation initiation. *Mol. Cell. Biol.*, **14**, 3208–3222.
15. Fogli,A. and Boespflug-Tanguy,O. (2006) The large spectrum of eIF2B-related diseases. *Biochem. Soc. Trans.*, **34**, 22–29.
16. Pavitt,G.D. and Proud,C.G. (2009) Protein synthesis and its control in neuronal cells with a focus on vanishing white matter disease. *Biochem. Soc. Trans.*, **37**, 1298–1310.
17. Gordiyenko,Y., Schmidt,C., Jennings,M.D., Matak-Vinkovic,D., Pavitt,G.D. and Robinson,C.V. (2014) eIF2B is a decameric guanine nucleotide exchange factor with a gamma2epsilon2 tetrameric core. *Nat. Commun.*, **5**, 3902.
18. Wortham,N.C., Martinez,M., Gordiyenko,Y., Robinson,C.V. and Proud,C.G. (2014) Analysis of the subunit organization of the eIF2B complex reveals new insights into its structure and regulation. *FASEB J.*, **28**, 2225–2237.
19. Wei,Z., Xue,Y., Xu,H. and Gong,W. (2006) Crystal structure of the C-terminal domain of S.cerevisiae eIF5. *J. Mol. Biol.*, **359**, 1–9.
20. Hiyama,T.B., Ito,T., Imataka,H. and Yokoyama,S. (2009) Crystal structure of the alpha subunit of human translation initiation factor 2B. *J. Mol. Biol.*, **392**, 937–951.
21. Bogorad,A.M., Xia,B., Sandor,D.G., Mamonov,A.B., Cafarella,T.R., Jehle,S., Vajda,S., Kozakov,D. and Marintchev,A. (2014) Insights into the architecture of the eIF2Balpha/beta/delta regulatory subcomplex. *Biochemistry*, **53**, 3432–3445.
22. Mueller,U., Darowski,N., Fuchs,M.R., Forster,R., Hellmig,M., Paithankar,K.S., Puhringer,S., Steffien,M., Zocher,G. and Weiss,M.S. (2012) Facilities for macromolecular crystallography at the Helmholtz-Zentrum Berlin. *J. Synchrotron. Radiat.*, **19**, 442–449.
23. McCoy,A.J., Grosse-Kunstleve,R.W., Adams,P.D., Winn,M.D., Storoni,L.C. and Read,R.J. (2007) Phaser crystallographic software. *J. Appl. Crystallogr.*, **40**, 658–674.
24. Adams,P.D., Afonine,P.V., Bunkoczi,G., Chen,V.B., Davis,I.W., Echols,N., Headd,J.J., Hung,L.W., Kapral,G.J., Grosse-Kunstleve,R.W. *et al.* (2010) PHENIX: a comprehensive Python-based system for macromolecular structure solution. *Acta Crystallogr. D Biol. Crystallogr.*, **66**, 213–221.
25. Emsley,P., Lohkamp,B., Scott,W.G. and Cowtan,K. (2010) Features and development of Coot. *Acta Crystallogr. D Biol. Crystallogr.*, **66**, 486–501.
26. Ericsson,U.B., Hallberg,B.M., Detitta,G.T., Dekker,N. and Nordlund,P. (2006) Thermofluor-based high-throughput stability

optimization of proteins for structural studies. *Anal. Biochem.*, **357**, 289–298.
27. Price,N.T., Mellor,H., Craddock,B.L., Flowers,K.M., Kimball,S.R., Wilmer,T., Jefferson,L.S. and Proud,C.G. (1996) eIF2B, the guanine nucleotide-exchange factor for eukaryotic initiation factor 2. Sequence conservation between the alpha, beta and delta subunits of eIF2B from mammals and yeast. *Biochem. J.*, **318**, 637–643.
28. Kakuta,Y., Tahara,M., Maetani,S., Yao,M., Tanaka,I. and Kimura,M. (2004) Crystal structure of the regulatory subunit of archaeal initiation factor 2B (aIF2B) from hyperthermophilic archaeon Pyrococcus horikoshii OT3: a proposed structure of the regulatory subcomplex of eukaryotic IF2B. *Biochem. Biophys. Res. Commun.*, **319**, 725–732.
29. Tamura,H., Saito,Y., Ashida,H., Inoue,T., Kai,Y., Yokota,A. and Matsumura,H. (2008) Crystal structure of 5-methylthioribose 1-phosphate isomerase product complex from Bacillus subtilis: implications for catalytic mechanism. *Protein Sci.*, **17**, 126–135.
30. Bumann,M., Djafarzadeh,S., Oberholzer,A.E., Bigler,P., Altmann,M., Trachsel,H. and Baumann,U. (2004) Crystal structure of yeast Ypr118w, a methylthioribose-1-phosphate isomerase related to regulatory eIF2B subunits. *J. Biol. Chem.*, **279**, 37087–37094.
31. Nakamura,A., Fujihashi,M., Aono,R., Sato,T., Nishiba,Y., Yoshida,S., Yano,A., Atomi,H., Imanaka,T. and Miki,K. (2012) Dynamic, ligand-dependent conformational change triggers reaction of ribose-1,5-bisphosphate isomerase from Thermococcus kodakarensis KOD1. *J. Biol. Chem.*, **287**, 20784–20796.
32. Liu,R., van der Lei,H.D., Wang,X., Wortham,N.C., Tang,H., van Berkel,C.G., Mufunde,T.A., Huang,W., van der Knaap,M.S., Scheper,G.C. *et al.* (2011) Severity of vanishing white matter disease does not correlate with deficits in eIF2B activity or the integrity of eIF2B complexes. *Hum. Mutat.*, **32**, 1036–1045.
33. Kyrpides,N.C. and Woese,C.R. (1998) Archaeal translation initiation revisited: the initiation factor 2 and eukaryotic initiation factor 2B alpha-beta-delta subunit families. *Proc. Natl. Acad. Sci. U.S.A.*, **95**, 3726–3730.
34. Dev,K., Santangelo,T.J., Rothenburg,S., Neculai,D., Dey,M., Sicheri,F., Dever,T.E., Reeve,J.N. and Hinnebusch,A.G. (2009) Archaeal aIF2B interacts with eukaryotic translation initiation factors eIF2alpha and eIF2Balpha: Implications for aIF2B function and eIF2B regulation. *J. Mol. Biol.*, **392**, 701–722.
35. Oldfield,S. and Proud,C.G. (1992) Purification, phosphorylation and control of the guanine-nucleotide-exchange factor from rabbit reticulocyte lysates. *Eur. J. Biochem.*, **208**, 73–81.
36. Dholakia,J.N., Francis,B.R., Haley,B.E. and Wahba,A.J. (1989) Photoaffinity labeling of the rabbit reticulocyte guanine nucleotide exchange factor and eukaryotic initiation factor 2 with 8-azidopurine nucleotides. Identification of GTP- and ATP-binding domains. *J. Biol. Chem.*, **264**, 20638–20642.
37. Dholakia,J.N., Mueser,T.C., Woodley,C.L., Parkhurst,L.J. and Wahba,A.J. (1986) The association of NADPH with the guanine nucleotide exchange factor from rabbit reticulocytes: a role of pyridine dinucleotides in eukaryotic polypeptide chain initiation. *Proc. Natl. Acad. Sci. U.S.A.*, **83**, 6746–6750.
38. Dholakia,J.N. and Wahba,A.J. (1989) Mechanism of the nucleotide exchange reaction in eukaryotic polypeptide chain initiation. Characterization of the guanine nucleotide exchange factor as a GTP-binding protein. *J. Biol. Chem.*, **264**, 546–550.
39. Kimball,S.R., Fabian,J.R., Pavitt,G.D., Hinnebusch,A.G. and Jefferson,L.S. (1998) Regulation of guanine nucleotide exchange through phosphorylation of eukaryotic initiation factor eIF2alpha. Role of the alpha- and delta-subunits of eiF2b. *J. Biol. Chem.*, **273**, 12841–12845.
40. Kyrpides,N.C. and Woese,C.R. (1998) Universally conserved translation initiation factors. *Proc. Natl. Acad. Sci. U.S.A.*, **95**, 224–228.
41. Marintchev,A. and Wagner,G. (2004) Translation initiation: structures, mechanisms and evolution. *Q. Rev. Biophys.*, **37**, 197–284.
42. Koonin,E.V. (1995) Multidomain organization of eukaryotic guanine nucleotide exchange translation initiation factor eIF-2B subunits revealed by analysis of conserved sequence motifs. *Protein Sci.*, **4**, 1608–1617.
43. Boesen,T., Mohammad,S.S., Pavitt,G.D. and Andersen,G.R. (2004) Structure of the catalytic fragment of translation initiation factor 2B and identification of a critically important catalytic residue. *J. Biol. Chem.*, **279**, 10584–10592.
44. Gomez,E., Mohammad,S.S. and Pavitt,G.D. (2002) Characterization of the minimal catalytic domain within eIF2B: the guanine-nucleotide exchange factor for translation initiation. *EMBO J.*, **21**, 5292–5301.
45. Hardie,D.G. (2014) AMP-activated protein kinase: maintaining energy homeostasis at the cellular and whole-body levels. *Annu. Rev. Nutr.*, **34**, 31–55.
46. Gross,M., Rubino,M.S. and Starn,T.K. (1988) Regulation of protein synthesis in rabbit reticulocyte lysate. Glucose 6-phosphate is required to maintain the activity of eukaryotic initiation factor (eIF)-2B by a mechanism that is independent of the phosphorylation of eIF-2 alpha. *J. Biol. Chem.*, **263**, 12486–12492.